



# Computational modeling of electrochemical coupling: A novel finite element approach towards ionic models for cardiac electrophysiology

Jonathan Wong<sup>a</sup>, Serdar Göktepe<sup>b</sup>, Ellen Kuhl<sup>c,\*</sup>

<sup>a</sup> Department of Mechanical Engineering, Stanford University, Stanford, CA 94305, USA

<sup>b</sup> Department of Civil Engineering, Middle East Technical University, 06531 Ankara, Turkey

<sup>c</sup> Departments of Mechanical Engineering, Bioengineering, and Cardiothoracic Surgery, Stanford University, Stanford, CA 94305, USA

## ARTICLE INFO

### Article history:

Received 22 December 2010

Received in revised form 24 May 2011

Accepted 12 July 2011

Available online 23 July 2011

### Keywords:

Nonlinear reaction–diffusion systems

Finite element method

Adaptive time stepping

Electrophysiology

Electrochemistry

Computational biophysics

## ABSTRACT

We propose a novel, efficient finite element solution technique to simulate the electrochemical response of excitable cardiac tissue. We apply a global–local split in which the membrane potential of the electrical problem is introduced globally as a nodal degree of freedom, while the state variables of the chemical problem are treated locally as internal variables on the integration point level. This particular discretization is efficient and highly modular since different cardiac cell models can be incorporated in a straightforward way through only minor local modifications on the constitutive level. Here, we derive the underlying algorithmic framework for a recently proposed ionic model for human ventricular cardiomyocytes, and demonstrate its integration into an existing nonlinear finite element infrastructure. To ensure unconditional algorithmic stability, we apply an implicit backward Euler scheme to discretize the evolution equations for both the electrical potential and the chemical state variables in time. To increase robustness and guarantee optimal quadratic convergence, we suggest an incremental iterative Newton–Raphson scheme and illustrate the consistent linearization of the weak form of the excitation problem. This particular solution strategy allows us to apply an adaptive time stepping scheme, which automatically generates small time steps during the rapid upstroke, and large time steps during the plateau, the repolarization, and the resting phases. We demonstrate that solving an entire cardiac cycle for a real patient-specific geometry characterized through a transmembrane potential, four ion concentrations, thirteen gating variables, and fifteen ionic currents requires computation times of less than ten minutes on a standard desktop computer.

© 2011 Elsevier B.V. All rights reserved.

## 1. Introduction

Despite intense research over the past decades, cardiovascular disease remains the single most common cause of natural death in developed nations [2,30]. Sudden cardiac death is estimated to account for approximately half of all these deaths, claiming approximately a thousand lives each day in the United States alone [12]. The high incidence and sudden, unexpected nature of sudden cardiac death, combined with the low success rate of resuscitation, make it a major unsolved problem in clinical cardiology, emergency medicine, and public health [10,69]. This manuscript is motivated by the vision to create a multi-scale patient-specific computational model of rhythm disorders in the heart to improve our understanding of the basic pathology associated with sudden cardiac death.

Since the famous experiments by Galvani [22] who impressively demonstrated the electrically stimulated contraction of

excised frog leg muscle more than two centuries ago, we have been trying to better understand the electrochemistry of living tissue. We now know that the electrophysiological activity of excitable cells is governed by a delicate balance between electrical and chemical gradients across the cell membrane [7]. These gradients are maintained by means of the membrane's selective permeability with respect to different ions at different points throughout an excitation cycle [5,23,42]. In cardiac cells, at rest, the transmembrane potential is approximately  $-86$  mV, meaning the cell's interior is negatively charged with respect to its exterior. Cardiac cells can be excited by an electrical stimulus that generates an initial depolarization across the cell membrane. Once this stimulus exceeds a certain threshold, the transmembrane potential increases rapidly from its resting state of approximately  $-86$  mV to its excited state of  $+20$  mV. After a brief period of partial initial repolarization, we can observe a characteristic plateau of about a fifth of a second before the cell gradually repolarizes to return to its original resting state [44], as illustrated in Fig. 1.

This characteristic temporal evolution of the transmembrane potential is brought about by the interaction of different ion channels controlling the inward and outward flux of charged

\* Corresponding author.

E-mail address: [ekuhl@stanford.edu](mailto:ekuhl@stanford.edu) (E. Kuhl).

URL: <http://biomechanics.stanford.edu> (E. Kuhl).

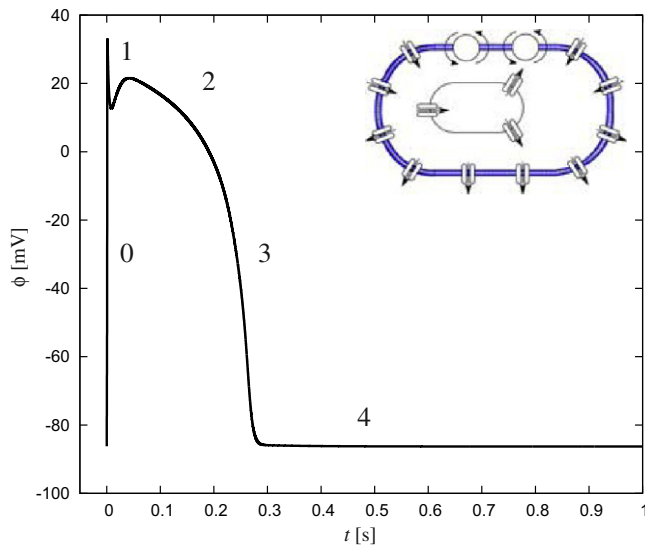


**Fig. 1.** Electrochemistry in a human ventricular cardiomyocyte. Time dependent evolution of transmembrane potential  $\phi$ . The characteristic action potential consists of five phases. Phase 0: The rapid upstroke is generated through an influx of positively charged sodium ions through fast sodium channels. Phase 1: Early, partial repolarization is initiated through the efflux of positively charged potassium ions through transient outward channels. Phase 2: During the plateau, the net influx of positively charged calcium ions through L-type sodium channels is balanced by the efflux of positively charged potassium ions through inward rectifier channels, rapid and slow delayed rectifier channels, and transient outward channels. Phase 3: Final repolarization begins when the efflux of potassium ions exceeds the influx of calcium ions. Phase 4: Throughout the interval between end of repolarization and the beginning of the next cycle the cell is at rest.

sodium, potassium, and calcium ions during the different phases of this excitation cycle. The first model to quantitatively describe the electrophysiological activity of excitable cells was proposed by Hodgkin and Huxley [29] who were awarded the Nobel Prize in Physiology and Medicine for their seminal work on action potentials in neurons half a century ago. In fact, most currently available cardiac cell models are derived from the classical Hodgkin–Huxley model. A significant conceptual simplification, the celebrated phenomenological two-parameter FitzHugh–Nagumo model [21,39], was proposed in the early 1960s to allow for a fundamental mathematical analysis of the coupling phenomena between electrical and chemical fields. In the 1970s, two sophisticated new mathematical models for the electrical activity of cardiac cells were introduced, one for cardiac Purkinje fibers [41,35] and one for mammalian ventricular cardiomyocytes [4]. The latter was calibrated by means of data from voltage-clamp experiments available at that time. Subsequent developments in single-cell and single-channel recording techniques enabled a more accurate control of intracellular and extracellular environments starting in the mid 1980s. These novel experimental techniques paved the way for a rigorous significant refinement of the earlier models for Purkinje fibers [20] and for mammalian ventricular cardiomyocytes [33]. The latter, the celebrated Luo–Rudy model [16,37,46], was originally calibrated for guinea pig ventricular cells [34], but soon thereafter adjusted to model human ventricular cardiomyocytes [6,17,45], and modified to incorporate intracellular calcium dynamics [28]. Here we will follow its most recent refinement, the ten Tusscher model [58,59] illustrated in Fig. 2, which we believe is extremely brilliant and powerful, however, unfortunately computationally demanding in its present explicit finite difference based form. Characterized through four ion concentrations, fifteen ionic currents, and thirteen gating variables, this model captures the essential characteristics of human ventricular cardiomyocytes: it contains the major ionic currents, includes basic intracellular calcium dynamics, and is well-calibrated against experimental

data [58–60]. The goal of this manuscript is therefore to develop an unconditionally stable, efficient, modular, flexible, and easily expandable algorithm for human ventricular cardiomyocytes motivated by the original ten Tusscher model and make it available for efficient whole heart simulations using common, existing finite element infrastructures.

Simulating the electrical activity of the heart is by no means new, and many established research groups have successfully contributed to solving this challenging task [43,48,53,61]. However, most cardiac excitation models are based on simplifying assumptions to capture the chemical activity on a phenomenological level, similar to the original FitzHugh–Nagumo model [47], as illustrated in various excellent overviews and monographs [14,31,50,59]. As one of the most efficient approaches, the distinguished two-parameter Aliev–Panfilov model [3] seeks to reproduce the major fundamental characteristics of the action potential at minimal computational cost. We have successfully implemented this model in a fully implicit nonlinear finite element framework in the past [24,26], applied it on patient-specific geometries to extract electrocardiograms [32], applied it in the context of bidomain formulations [18], and coupled it to mechanical contraction in a monolithic whole heart simulation [25]. In this manuscript, rather than using a phenomenological model, we seek to investigate the potential of ionic models in the context of our previously proposed generic finite element framework [24], embedded in the multipurpose nonlinear finite element program FEAP [55] and its recent parallel version [56]. Within this generic framework, all chemical state variables, in our case the four ion concentrations and the thirteen gating variables, are introduced locally as internal variables on the integration point level.

This manuscript is organized as follows: Section 2 briefly summarizes the governing equations of the electrical excitation problem and the chemical ion concentration problem. Section 3 then illustrates the computational solution algorithm based on a global node point based solution of the electrical excitation problem combined with a local integration point based solution of the chemical concentration problem. In Section 4 we specify the constitutive equations for the particular model problem of a human ventricular cardiomyocyte characterized through thirteen gating variables, fifteen ionic currents, and four ion concentrations which we integrate into the discrete framework in Section 5. Section 6 documents the features of the proposed algorithm in the context of a single human ventricular cardiomyocyte in Section 6.1 and in terms of a real human heart geometry in Section 6.2. We close with a final discussion and an outlook with future directions in Section 7. Mathematical details about the algorithmic formulation are provided in Appendix A.

## 2. Continuous problem of electrochemistry

In this section, we summarize the generic equations of electrochemical coupling in cardiac tissue characterized through a partial differential equation for the electrical problem and through a system of ordinary differential equations for the chemical problem [16,38,46,64]. We then specify the generic set of equations to represent a particular ionic model of a human ventricular cardiomyocyte [4,28,33,58]. The primary unknown of the electrical problem is the membrane potential  $\phi$ , the unknowns of the chemical problem are the state variables, i.e., the  $n_{\text{gate}}$  gating variables  $g_{\text{gate}}$  and the  $n_{\text{ion}}$  ion concentrations  $c_{\text{ion}}$ .

### 2.1. Electrical problem – partial differential equation

The excitation problem is characterized through the spatio-temporal evolution of the membrane potential  $\phi$  in terms of the flux term  $\text{div} \mathbf{q}$  and the source term  $f^{\text{pb}}$ .

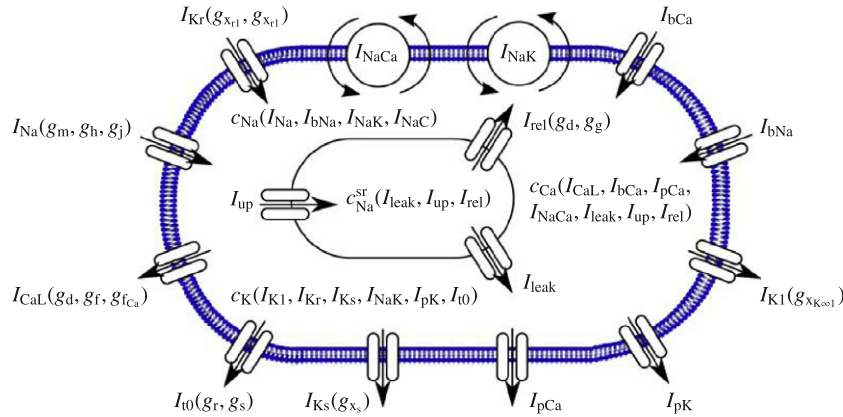


**Fig. 2.** Ionic model of a human ventricular cardiomyocyte [4,28,33,58]. In this model, the electrochemical state of the cardiomyocyte is characterized in terms of  $n_{ion} = 4$  ion concentrations, the free intracellular sodium, potassium, and calcium concentrations and the free calcium concentration in the sarcoplasmic reticulum,  $c_{ion} = [c_{Na}, c_K, c_{Ca}, c_{Ca}^{sr}]$ . Ion concentrations are controlled through  $n_{crt} = 15$  ionic currents,  $I_{crt} = [I_{Na}, I_{bNa}, I_{NaK}, I_{NaCa}, I_{K1}, I_{Kr}, I_{Ks}, I_{pK}, I_{t0}, I_{CaL}, I_{bCa}, I_{pCa}, I_{leak}, I_{up}, I_{rel}]$ . Their channels are governed by  $n_{gate} = 13$  gating variables  $g_{gate} = [g_m, g_h, g_j, g_{xK1\infty}, g_{xr1}, g_{xr2}, g_{xs}, g_r, g_s, g_d, g_f, g_{fCa}, g_g]$  which are functions of the current membrane potential  $\phi$ .

$$\dot{\phi} = \text{div } \mathbf{q}(\phi) + f^\phi(\phi, \mathbf{g}_{gate}, c_{ion}). \quad (1)$$

It has become common practice to enhance the initially local equation for cellular excitation by a phenomenological membrane potential flux  $\text{div } \mathbf{q}$  with

$$\mathbf{q} = \mathbf{D} \cdot \nabla \phi, \quad (2)$$

to account for the nonlocal nature of propagating excitation waves. Membrane potential propagation is characterized through the second order diffusion tensor  $\mathbf{D} = d_{iso} \mathbf{I} + d_{ani} \mathbf{n} \otimes \mathbf{n}$  related to the gap junctions between the cells. The diffusion tensor can account for both isotropic propagation  $d_{iso}$  and anisotropic propagation  $d_{ani}$  along preferred directions  $\mathbf{n}$ . The source term

$$f^\phi = - \sum_{crt=1}^{n_{crt}} I_{crt}(\phi, \mathbf{g}_{gate}, c_{ion}) \quad (3)$$

is basically directly related to the negative sum of the  $n_{crt}$  ionic currents  $I_{crt}$  across the cell membrane. Chemolectrical coupling is introduced through these ionic currents which are parameterized in terms of the gating variables  $g_{gate}$  and ion concentrations  $c_{ion}$ . The evolution of these chemical state variables will be characterized in detail in the following subsection.

### 2.2. Chemical problem – system of ordinary differential equations

From a mathematical point of view, the chemical problem is defined in terms of two sets of ordinary differential equations, one for the  $n_{gate}$  gating variables  $g_{gate}$  and one for the  $n_{ion}$  ion concentrations  $c_{ion}$  [16,37,46,66]. The gating variables essentially characterize the states of the individual ion channels, which can be either open or closed. It proves convenient to divide the gating variables into two subsets, a first set  $g_{gate}^I$  which depends only on the current membrane potential  $\phi$ , and a second set  $g_{gate}^{II}$  which depends on both the membrane potential  $\phi$  and the corresponding ion concentration  $c_{ion}$ . The gating variables are defined through the following set of ordinary differential equations.

$$\begin{aligned} \dot{g}_{gate}^I &= f_{gate}^{gI}(\phi, g_{gate}^I) = \frac{1}{\tau_{gate}^I(\phi)} [g_{gate}^{\infty I}(\phi) - g_{gate}^I], \\ \dot{g}_{gate}^{II} &= f_{gate}^{gII}(\phi, g_{gate}^{II}, c_{ion}) = \frac{1}{\tau_{gate}^{II}(\phi)} [g_{gate}^{\infty II}(\phi, c_{ion}) - g_{gate}^{II}]. \end{aligned} \quad (4)$$

Their evolution is governed by classical Hodgin–Huxley type equations, each characterized through a steady-state value  $g_{gate}^{\infty}$  and a

time constant  $\tau_{gate}$  for reaching this steady state, where both are usually exponential functions of the membrane potential  $\phi$ . In addition, the steady state values of the second set  $g_{gate}^{\infty II}$  are also functions of the ion concentration  $c_{ion}$ . The relevant ion concentrations in cardiac cells are typically the sodium concentration  $c_{Na}$ , the potassium concentration  $c_K$ , the calcium concentration  $c_{Ca}$ , and, in our case, the calcium concentration in the sarcoplasmic reticulum  $c_{Ca}^{sr}$ . Collectively, these ion concentrations  $c_{ion}$  are defined through a second set of ordinary differential equations.

$$\dot{c}_{ion} = f_{ion}^c(\phi, \mathbf{g}_{gate}, c_{ion}). \quad (5)$$

Their evolution is driven by the individual righthand sides  $f_{ion}^c$ , which represent nothing but the weighted sums of the corresponding individual transmembrane currents  $I_{crt}$ . These  $n_{crt}$  ionic currents

$$I_{crt} = I_{crt}(\phi, \mathbf{g}_{gate}, c_{ion}), \quad (6)$$

can be expressed in terms of the current potential, the set of gating variables, and the set of ion concentrations. Electrochemical coupling is thus introduced through the voltage-gated nature of the relevant ion channels which reflects itself in the potential-dependency of the chemical state variables  $g_{gate}$  and  $c_{ion}$ . The particular cell model illustrated in Fig. 2, which we will explain in detail in Section 4, is characterized in terms of  $n_{ion} = 4$  ion concentrations  $c_{ion} = [c_{Na}, c_K, c_{Ca}, c_{Ca}^{sr}]$ ,  $n_{crt} = 15$  ionic currents  $I_{crt} = [I_{Na}, I_{bNa}, I_{NaK}, I_{NaCa}, I_{K1}, I_{Kr}, I_{Ks}, I_{pK}, I_{t0}, I_{CaL}, I_{bCa}, I_{pCa}, I_{leak}, I_{up}, I_{rel}]$ , and  $n_{gate} = 13$  gating variables  $g_{gate}^I = [g_m, g_h, g_j, g_{xr1}, g_{xr2}, g_{xs}, g_r, g_s, g_d, g_f]$  and  $g_{gate}^{II} = [g_{xK1\infty}, g_{fCa}, g_g]$ . It is obvious that the complex, nonlinear coupled system of equations for the membrane potential, the gating variables, and the ion concentrations cannot be solved analytically. In the following section, we will illustrate the discrete problem of electrochemical coupling introducing a consistently linearized fully implicit finite element solution scheme based on a global–local split.

### 3. Discrete problem of electrochemistry

We suggest discretizing the spatio-temporal problem of electrochemical coupling (1), (4) and (5) for the transmembrane potential  $\phi$ , the gating variables  $g_{gate}$ , and the intracellular ion concentrations  $c_{ion}$  with a finite difference scheme in time and with a finite element scheme in space. Due to the global nature of the membrane potential introduced through the diffusion term  $\text{div } \mathbf{q}(\phi)$ , we propose a  $C^0$ -continuous finite element interpolation for the

membrane potential  $\phi$ , while a  $C^{-1}$ -continuous interpolation is sufficient for the sets of gating variables  $g_{\text{gate}}$  and ion concentrations  $c_{\text{ion}}$ . Accordingly, we introduce the membrane potential as global degree of freedom at each finite element node, whereas the gating variables and ion concentrations are introduced locally on the integration point level. The resulting staggered system is solved with an incremental iterative Newton–Raphson solution procedure based on the consistent linearization of the discrete excitation problem [24–26,32]. The use of a fully monolithic implicit solution algorithm allows us to apply an adaptive time stepping procedure, for which the time step size is automatically adjusted in response to the number of Newton iterations towards global equilibrium [55].

### 3.1. Electrical problem – global discretization on the node point level

Let us first transform the electrical problem (1) into its residual format

$$R^\phi = \dot{\phi} - \text{div}(\mathbf{q}) - f^\phi \doteq 0 \quad \text{in } \mathcal{B} \quad (7)$$

which we complement by the corresponding Dirichlet and Neumann boundary conditions  $\phi = \bar{\phi}$  on  $\partial\mathcal{B}_\phi$  and  $\mathbf{q} \cdot \mathbf{n} = \bar{q}$  on  $\partial\mathcal{B}_q$ . For most physiologically relevant excitation problems, homogeneous Neumann boundary conditions  $\mathbf{q} \cdot \mathbf{n} = 0$  are applied on the entire boundary  $\partial\mathcal{B}$ . As initial conditions,  $\phi_0(x) = \phi(x, t_0)$  in  $\mathcal{B}$ , we typically set the transmembrane potential to its resting state. The weak form of the electrical residual (7) is obtained by the integration over the domain  $\mathcal{B}$ , the standard integration by parts, and the inclusion of the Neumann boundary conditions. For the spatial discretization, we discretize the domain of interest  $\mathcal{B}$  with  $n_{\text{el}}$  finite elements  $\mathcal{B}^e$  as  $\mathcal{B} = \bigcup_{e=1}^{n_{\text{el}}} \mathcal{B}^e$  and apply the standard isoparametric concept to interpolate the trial functions  $\phi^h$  and the test functions  $\delta\phi^h$ .

$$\delta\phi^h|_{\mathcal{B}^e} = \sum_{i=1}^{n_{\text{en}}} N^i \delta\phi_i, \quad \phi^h|_{\mathcal{B}^e} = \sum_{j=1}^{n_{\text{en}}} N^j \phi_j. \quad (8)$$

Here,  $N$  are the standard shape functions on the element level and  $i, j = 1, \dots, n_{\text{en}}$  are the  $n_{\text{en}}$  element nodes. For the temporal discretization, we partition the time interval of interest  $\mathcal{T}$  into  $n_{\text{stp}}$  subintervals  $[t^n, t^{n+1}]$  as  $\mathcal{T} = \bigcup_{n=0}^{n_{\text{stp}}-1} [t^n, t^{n+1}]$  and apply a standard backward Euler time integration scheme in combination with a finite difference approximation of the first order time derivative  $\dot{\phi}$ .

$$\dot{\phi} = [\phi - \phi^n] / \Delta t \quad (9)$$

Herein, the index  $(\circ)^{n+1}$  has been omitted for the sake of clarity, and the common abbreviation  $\Delta t := t - t^n > 0$  has been introduced for the current time increment. With the discretizations in space (8) and time (9), the discrete algorithmic residual  $R_I^\phi$  takes the following explicit representation.

$$R_I^\phi = \mathbf{A}_{e=1}^{n_{\text{el}}} \int_{\mathcal{B}^e} N^i \frac{\phi - \phi^n}{\Delta t} + \nabla N^i \cdot \mathbf{q} \, dV - \int_{\partial\mathcal{B}_q^e} N^i \bar{q} \, dA - \int_{\mathcal{B}^e} N^i f^\phi \, dV \doteq 0. \quad (10)$$

The operator  $\mathbf{A}$  symbolizes the assembly of all element contributions at the element nodes  $i = 1, \dots, n_{\text{en}}$  to the overall residual at the global node points  $I = 1, \dots, n_{\text{nd}}$ . To solve the discrete system of nonlinear Eq. (10), we suggest an incremental iterative Newton Raphson solution technique based on the consistent linearization of the residual which introduces the global iteration matrix  $K_{ij}^\phi$ .

$$K_{ij}^\phi = \mathbf{d}_{\phi_j} R_I^\phi = \mathbf{A}_{e=1}^{n_{\text{el}}} \int_{\mathcal{B}^e} N^i \frac{1}{\Delta t} N^j + \nabla N^i \cdot \mathbf{D} \cdot \nabla N^j - N^i \mathbf{d}_{\phi_j} f^\phi N^j \, dV. \quad (11)$$

For each incremental iteration, we update the global vector of unknowns  $\phi_I \leftarrow \phi_I - \sum_{j=1}^{n_{\text{nd}}} K_{ij}^{\phi-1} R_j^\phi$  at all  $I = 1, \dots, n_{\text{nd}}$  global nodes.

In the following subsection, we illustrate the iterative calculation of the source term  $f^\phi(\phi, g_{\text{gate}}, c_{\text{ion}})$  and its consistent algorithmic linearization  $\mathbf{d}_{\phi_j} f^\phi(\phi, g_{\text{gate}}, c_{\text{ion}})$  required to evaluate the global residual (10) and the global iteration matrix (11).

### 3.2. Chemical problem – local discretization on the integration point level

The chemical problem is characterized through  $n_{\text{gate}}$  gating variables  $g_{\text{gate}}^I$  and  $g_{\text{gate}}^{II}$ , and  $n_{\text{ion}}$  ion concentrations  $c_{\text{ion}}$  which we introduce as internal variables to be stored locally on the integration point level. We typically initialize the chemical state variables at  $t_0$  with their resting state values. For their advancement in time, we suggest a finite difference approximation for their temporal discretization,

$$\begin{aligned} \dot{g}_{\text{gate}}^I &= [g_{\text{gate}}^I - g_{\text{gate}}^{In}] / \Delta t, \\ \dot{g}_{\text{gate}}^{II} &= [g_{\text{gate}}^{II} - g_{\text{gate}}^{IIIn}] / \Delta t, \quad \dot{c}_{\text{ion}} = [c_{\text{ion}} - c_{\text{ion}}^n] / \Delta t \end{aligned} \quad (12)$$

and apply the classical implicit backward Euler scheme to transform the linear set of gating Eq. (4) into a set of update equations for the gating variables  $g_{\text{gate}}^I$  and  $g_{\text{gate}}^{II}$  at the current time step  $t$ .

$$\begin{aligned} g_{\text{gate}}^I &= g_{\text{gate}}^{In} + \frac{1}{\tau_{\text{gate}}^I(\phi)} [g_{\text{gate}}^{\infty I}(\phi) - g_{\text{gate}}^I] \Delta t, \\ g_{\text{gate}}^{II} &= g_{\text{gate}}^{IIIn} + \frac{1}{\tau_{\text{gate}}^{II}(\phi)} [g_{\text{gate}}^{\infty II}(\phi, c_{\text{ion}}) - g_{\text{gate}}^{II}] \Delta t. \end{aligned} \quad (13)$$

Both sets are initialized based on the current membrane potential  $\phi$ . While the first set remains constant throughout the remainder of the constitutive subroutine, the second set is updated iteratively throughout the subsequent local Newton iterations. The gating variables essentially define the  $n_{\text{crt}}$  ionic currents  $I_{\text{crt}}(\phi, g_{\text{gate}}, c_{\text{ion}})$  which alter the intracellular ion concentrations through the righthand sides  $f_{\text{ion}}^c$  of Eq. (5). With the help of the finite difference approximation (12), the nonlinear set of concentration Eq. (5), which constitutes the core of the chemical problem, is restated in the following residual format.

$$R_{\text{ion}}^c = c_{\text{ion}} - c_{\text{ion}}^n - f_{\text{ion}}^c(\phi, g_{\text{gate}}, c_{\text{ion}}) \Delta t \doteq 0. \quad (14)$$

The discrete algorithmic residual is linearized consistently to yield the  $n_{\text{ion}} \times n_{\text{ion}}$  iteration matrix  $K_{\text{ion ion}}^c$  for the local Newton iteration on the integration point level.

$$K_{\text{ion ion}}^c = \mathbf{d}_{c_{\text{ion}}} R_{\text{ion}}^c. \quad (15)$$

At the end of each Newton iteration, we update the set of ion concentrations  $c_{\text{ion}} \leftarrow c_{\text{ion}} - [K_{\text{ion ion}}^c]^{-1} R_{\text{ion}}^c$ , the second set of gating variables  $g_{\text{gate}}^{II} \leftarrow g_{\text{gate}}^{IIIn} + f_{\text{gate}}^{II}(\phi, g_{\text{gate}}, c_{\text{ion}}) \Delta t$  and the set of ionic currents  $I_{\text{crt}} \leftarrow I_{\text{crt}}(\phi, g_{\text{gate}}, c_{\text{ion}})$ . At convergence, i.e., at chemical equilibrium, we can finally calculate the source term  $f^\phi(\phi, g_{\text{gate}}, c_{\text{ion}})$  for the electrical problem (10), and its linearization  $\mathbf{d}_{\phi_j} f^\phi(\phi, g_{\text{gate}}, c_{\text{ion}})$  for the global Newton iteration (11). Table 1 illustrates the algorithmic solution of the coupled electrochemical problem with its characteristic local–global split. Its local inner loop can be understood as a modern implicit version of the iterative update procedure of the original Rush–Larsen algorithm [49]. Note that, in principle, we could solve for all our internal variables, i.e., for all  $n_{\text{gate}}$  gating variables and for all  $n_{\text{ion}}$  ionic concentrations simultaneously. This would require to invert a  $[n_{\text{gate}} + n_{\text{ion}}] \times [n_{\text{gate}} + n_{\text{ion}}]$  iteration matrix, in our case a  $17 \times 17$  matrix, for each local Newton iteration, at each integration point, during each global iteration step, for each time increment. Because of the particular interdependence of the internal variables, however, we can first update the first set of gating variables  $g_{\text{gate}}^I$  that only depend on the current membrane potential  $\phi$ , but not on any other internal variables. Then, we calculate the coupled set of ion concentrations  $c_{\text{ion}}$  which is characterized only

**Table 1**

Algorithmic treatment of electrochemical coupling in excitable cardiac tissue based on finite element discretization in space and implicit finite difference discretization in time embedded in two nested Newton–Raphson iterations. The electrical unknown, the membrane potential  $\phi$ , is introduced globally on the node point level whereas the chemical unknowns, the two sets of gating variables  $g_{\text{gate}}^I$  and  $g_{\text{gate}}^{II}$  and the ion concentrations  $c_{\text{ion}}$  are introduced locally on the integration point level.

initialize nodal degrees of freedom $\phi_J$
initialize internal variables $g_{\text{gate}}^I, g_{\text{gate}}^{II}, c_{\text{ion}}$
global Newton iteration
loop over all elements
loop over all integration points
update first set of gating variables $g_{\text{gate}}^I \leftarrow g_{\text{gate}}^I + f_{\text{gate}}^{gI} \Delta t$ (23, 24, 25, 29, 30, 31, 32, 33, 36, 37)
initialize second set of gating variables $g_{\text{gate}}^{II} \leftarrow g_{\text{gate}}^{II} + f_{\text{gate}}^{gII} \Delta t$ (28, 38, 39)
initialize ionic currents $I_{\text{crt}} \leftarrow I_{\text{crt}}(\phi, g_{\text{gate}}^I, g_{\text{gate}}^{II}, c_{\text{ion}})$ (22, 27, 35, 41)
local Newton iteration
calculate ion concentration residuals $R_{\text{ion}}^c$ and local iteration matrix $[K_{\text{ion ion}}^c] = d_{c_{\text{ion}}} R_{\text{ion}}^c$ (42, 43)
update ion concentrations $c_{\text{ion}} \leftarrow c_{\text{ion}} - [K_{\text{ion ion}}^c]^{-1} R_{\text{ion}}^c$
update second set of gating variables $g_{\text{gate}}^{II} \leftarrow g_{\text{gate}}^{II} + f_{\text{gate}}^{gII} \Delta t$ (28, 38, 39)
update ionic currents $I_{\text{crt}} \leftarrow I_{\text{crt}}(\phi, g_{\text{gate}}^I, g_{\text{gate}}^{II}, c_{\text{ion}})$ (22, 27, 35, 41)
calculate source term $f^\phi(I_{\text{crt}})$ and its linearization $d_\phi f^\phi$ (44, 45)
calculate element residuals $R_I^{\phi e}$ and element matrices $K_{IJ}^{\phi e} = d_{\phi_j^e} R_I^{\phi e}$ (10, 11)
calculate global residual $R_I^\phi$ and global iteration matrix $K_{IJ}^\phi = d_{\phi_j} R_I^\phi$ (10, 11)
update membrane potential $\phi_J \leftarrow \phi_J - K_{IJ}^{\phi-1} R_I^\phi$

through a  $n_{\text{ion}} \times n_{\text{ion}}$  iteration matrix, in our case a  $4 \times 4$  matrix. Last, we update the second set of gating variables  $g_{\text{gate}}^{II}$ , which then only depends on previously calculated internal variables. Table 1 illustrates the local update algorithm tailored to this particular interdependence of internal variables. Overall, this local update is fully implicit.

#### 4. Continuous model problem for human ventricular cardiomyocytes

In this section, we will specify the constitutive equations of electrochemistry for an enhanced version of the classical Luo–Rudy model for ventricular cardiomyocytes [33,34] that incorporates recently proposed modifications [28,45,58,60] as illustrated in Fig. 2. This model is characterized through  $n_{\text{ion}} = 4$  ion concentrations,

$$\dot{c}_{\text{ion}} = \dot{c}_{\text{ion}}(\phi, g_{\text{gate}}, c_{\text{ion}}) \quad \text{with} \quad c_{\text{ion}} = [c_{\text{Na}}, c_{\text{K}}, c_{\text{Ca}}, c_{\text{Ca}}^{\text{sr}}], \quad (16)$$

where  $c_{\text{Na}}$ ,  $c_{\text{K}}$ , and  $c_{\text{Ca}}$  are the intracellular sodium, potassium, and calcium concentration, and  $c_{\text{Ca}}^{\text{sr}}$  is the calcium concentration in the sarcoplasmic reticulum. Fig. 2 illustrates the  $n_{\text{crt}} = 15$  ionic currents of the model.

$$I_{\text{crt}} = I_{\text{crt}}(\phi, g_{\text{gate}}, c_{\text{ion}}) \quad \text{with} \\ I_{\text{crt}} = [I_{\text{Na}}, I_{\text{bNa}}, I_{\text{NaK}}, I_{\text{NaCa}}, I_{\text{K1}}, I_{\text{Kr}}, I_{\text{Ks}}, I_{\text{pK}}, I_{\text{t0}}, I_{\text{CaL}}, I_{\text{bCa}}, I_{\text{pCa}}, I_{\text{leak}}, I_{\text{up}}, I_{\text{rel}}]. \quad (17)$$

In particular, the sodium related currents  $I_{\text{Na}}, I_{\text{bNa}}, I_{\text{NaK}}, I_{\text{NaCa}}$  induce changes in the intracellular sodium concentration  $c_{\text{Na}}$ , the potassium related currents  $I_{\text{K1}}, I_{\text{Kr}}, I_{\text{Ks}}, I_{\text{NaK}}, I_{\text{pK}}, I_{\text{t0}}$  induce changes in the intracellular potassium concentration  $c_{\text{K}}$ , the calcium related

currents  $I_{\text{CaL}}, I_{\text{bCa}}, I_{\text{pCa}}, I_{\text{NaCa}}, I_{\text{leak}}, I_{\text{up}}, I_{\text{rel}}$  induce changes in the intracellular calcium concentration  $c_{\text{Ca}}$ , and the calcium related currents  $I_{\text{leak}}, I_{\text{up}}, I_{\text{rel}}$  induce changes in the calcium concentration in the sarcoplasmic reticulum  $c_{\text{Ca}}^{\text{sr}}$ , respectively. The states of the channels associated with these currents are gated by  $n_{\text{gate}} = 13$  gating variables,

$$\dot{g}_{\text{gate}}^I = \dot{g}_{\text{gate}}^I(\phi, g_{\text{gate}}^I), \\ \dot{g}_{\text{gate}}^{II} = \dot{g}_{\text{gate}}^{II}(\phi, g_{\text{gate}}^{II}, c_{\text{ion}}), \quad (18)$$

with

$$g_{\text{gate}}^I = [g_{\text{m}}, g_{\text{h}}, g_{\text{j}}, g_{\text{xr1}}, g_{\text{xr2}}, g_{\text{xs}}, g_{\text{r}}, g_{\text{s}}, g_{\text{d}}, g_{\text{f}}], \\ g_{\text{gate}}^{II} = [g_{\text{K1}\infty}, g_{\text{fCa}}, g_{\text{g}}]$$

with  $g_{\text{m}}, g_{\text{h}}, g_{\text{j}}$  gating  $I_{\text{Na}}$ , the fast sodium channel,  $g_{\text{K1}\infty}$  gating  $I_{\text{K1}}$ , the inward rectifier channel,  $g_{\text{xr1}}, g_{\text{xr2}}$  gating  $I_{\text{Kr}}$ , the rapid delayed rectifier channel,  $g_{\text{xs}}$  gating  $I_{\text{Ks}}$ , the slow delayed rectifier channel,  $g_{\text{r}}, g_{\text{s}}$  gating  $I_{\text{t0}}$ , the transient outward channel,  $g_{\text{d}}, g_{\text{f}}, g_{\text{fCa}}$  gating  $I_{\text{CaL}}$ , the L-type calcium channel, and  $g_{\text{d}}, g_{\text{g}}$  gating  $I_{\text{rel}}$ , the sarcoplasmic reticulum calcium release channel, respectively, see Fig. 2. For each ion, sodium, potassium, and calcium, we can evaluate the classical Nernst equation,

$$\phi_{\text{ion}} = \frac{RT}{z_{\text{ion}}F} \log \left( \frac{c_{\text{ion0}}}{c_{\text{ion}}} \right) \quad \text{with} \quad \phi_{\text{ion}} = [\phi_{\text{Na}}, \phi_{\text{K}}, \phi_{\text{Ca}}], \quad (19)$$

to determine the concentration-dependent Nernst or reversal potential  $\phi_{\text{ion}}$ , which corresponds to the potential difference across

**Table 2**  
Material parameters of the proposed human ventricular cardiomyocyte model [28,33,45,58].

	Sodium related	Potassium related	Calcium related	Calcium <sup>sr</sup> related
Concentrations	$c_{Na0} = 140$ mM	$c_{K0} = 5.4$ mM	$c_{Ca0} = 2$ mM	–
Maximum currents	$I_{NaCa}^{max} = 1000$ pA/pF $I_{NaK}^{max} = 1.362$ pA/pF	$I_{NaCa}^{max} = 1000$ pA/pF $I_{NaK}^{max} = 1.362$ pA/pF	$I_{leak}^{max} = 0.08$ s <sup>-1</sup> $I_{up}^{max} = 0.425$ mM/s $I_{rel}^{max} = 8.232$ mM/s	$I_{leak}^{max} = 0.08$ s <sup>-1</sup> $I_{rel}^{max} = 0.425$ mM/s $I_{rel}^{max} = 8.232$ mM/s
Maximum conductances	$C_{Na}^{max} = 14.838$ nS/pF $C_{bNa}^{max} = 0.00029$ nS/pF	$C_{K1}^{max} = 5.405$ nS/pF $C_{Kr}^{max} = 0.0096$ nS/pF $C_{Ks,epi}^{max} = 0.245$ nS/pF $C_{Ks,endo}^{max} = 0.245$ nS/pF $C_{Ks,M}^{max} = 0.062$ nS/pF $C_{pK}^{max} = 0.0146$ nS/pF $C_{t0,epi}^{max} = 0.294$ nS/pF $C_{t0,endo}^{max} = 0.073$ nS/pF $C_{t0,M}^{max} = 0.294$ nS/pF	$C_{CaL}^{max} = 0.175$ mm <sup>3</sup> /[μFs] $C_{bCa}^{max} = 0.000592$ nS/pF $C_{pCa}^{max} = 0.825$ nS/pF	
Half saturation constants	$C_{CaNa} = 1.38$ mM $C_{NaCa} = 87.50$ mM $C_{KNa} = 1.00$ mM $C_{NaK} = 40.00$ mM	$C_{KNa} = 1.00$ mM $C_{NaK} = 40.00$ mM	$C_{CaNa} = 1.38$ mM $C_{NaCa} = 87.50$ mM $C_{pCa} = 0.0005$ mM $C_{up} = 0.00025$ mM $C_{rel} = 0.25$ mM $C_{buf} = 0.001$ mM	$C_{up} = 0.00025$ mM $C_{rel} = 0.25$ mM $C_{buf}^{sr} = 0.3$ mM
Other parameters	$k_{NaCa}^{sat} = 0.10$ $\gamma_{NaCa} = 2.50$ $\gamma = 0.35$	$p_{KNa} = 0.03$	$\gamma_{rel} = 2$ $C_{tot} = 0.15$ mM	$\gamma_{rel} = 2$ $C_{tot}^{sr} = 10$ mM
Gas constant $R = 8.3143$ J K <sup>-1</sup> mol <sup>-1</sup> Faraday constant $F = 96.4867$ C/mmol		Temperature $T = 310$ K Membrane capacitance $C = 185$ pF	Cytoplasmic volume $V = 16,404$ μm <sup>3</sup> Sarcoplasmic reticulum volume $V^{sr} = 1094$ μm <sup>3</sup>	

the cell membrane that would be generated by this particular ion if no other ions were present. This implies that at times when the membrane is particularly permeable to a specific ion, its overall membrane potential  $\phi$  tends to approach this ion's equilibrium potential  $\phi_{ion}$ . In the Nernst equation (19),  $R = 8.3143$  J K<sup>-1</sup> mol<sup>-1</sup> is the gas constant,  $T = 310$  K is the absolute temperature, and  $F = 96.4867$  C/mmol is the Faraday constant. The constant  $z_{ion}$  is the elementary charge per ion, i.e.,  $z_{Na} = 1$ ,  $z_K = 1$ , for singly-charged sodium and potassium ions and  $z_{Ca} = 2$  for doubly-charged calcium ions. The extracellular sodium, potassium, and calcium concentrations are given as  $c_{Na0} = 140$  mM,  $c_{K0} = 5.4$  mM, and  $c_{Ca0} = 2$  mM, respectively, and  $c_{ion}$  denotes the corresponding intracellular ion concentration. In the following subsections, we will specify the individual concentrations, currents, and gating variables for sodium, potassium, and calcium. These will allow us to define the source term  $f^{\phi}$  for the electrical problem (3).

$$f^{\phi} = -[I_{Na} + I_{bNa} + I_{NaK} + I_{NaCa} + I_{K1} + I_{Kr} + I_{Ks} + I_{pK} + I_{t0} + I_{CaL} + I_{bCa} + I_{pCa}]. \quad (20)$$

Throughout the remainder of the manuscript, physical units will be used throughout, with time  $t$  given in milliseconds, voltage  $\phi$  given in millivolts, ionic currents across the cell membrane given in picoamperes per picofarad, ionic currents across the membrane of the sarcoplasmic reticulum given in millimolar per millisecond, conductances  $C_{crt}$  given in nanosiemens per picofarad, and intracellular and extracellular ion concentrations  $c_{ion}$  given in millimoles per liter. For the sake of completeness, all material parameters of the human ventricular cardiomyocyte model [28,33,45,58] are summarized in Table 2.

#### 4.1. Specification of sodium concentration, currents, and gating variables

Sodium plays a crucial role in generating the fast upstroke in the initial phase of the action potential. At rest, the intracellular

sodium concentration is approximately  $c_{Na} = 11.6$  mM, which implies that, according to Eq. (19), the sodium equilibrium potential is  $\phi_{Na} = +66.5$  mV. Accordingly, both electrical forces and chemical gradients pull extracellular sodium ions into the cell. The influx of sodium ions is small, however, since at rest, the membrane is relatively impermeable to sodium. Through an external stimulus above a critical threshold value, the fast sodium channels are opened to initiate a rapid inflow of sodium ions associated with the rapid depolarization of the cell membrane. The transmembrane potential increases drastically by more than 100 mV in less than 2 ms, see Fig. 2. At the end of the upstroke, the cell membrane is positively charged, and the fast sodium channels return to their closed state. In our specific model problem of human ventricular cardiomyocytes, the sodium concentration

$$\dot{c}_{Na} = -\frac{C}{VF}[I_{Na} + I_{bNa} + 3I_{NaK} + 3I_{NaCa}] \quad (21)$$

is evolving in response to the fast sodium current  $I_{Na}$ , the background sodium current  $I_{bNa}$ , the sodium potassium pump current  $I_{NaK}$ , and the sodium calcium exchanger current  $I_{NaCa}$ , scaled by the membrane capacitance per unit surface area  $C = 185$  pF, the cytoplasmic volume  $V = 16,404$  μm<sup>3</sup>, and the Faraday constant  $F = 96.4867$  C/mmol. Note that both the sodium potassium pump and the sodium calcium exchanger operate at a three-to-two ratio as indicated by the scaling factor three. The sodium related currents are defined as follows,

$$\begin{aligned} I_{Na} &= C_{Na}^{max} g_m g_h g_j [\phi - \phi_{Na}], \\ I_{bNa} &= C_{bNa}^{max} [\phi - \phi_{Na}] \\ I_{NaK} &= I_{NaK}^{max} [C_{K0} c_{Na}] [C_{Na} + C_{NaK}] [C_{K0} + C_{KNa}] \\ &\quad \times [1 + 0.1245e^{-0.1\phi/RT} + 0.0353e^{-\phi/RT}]^{-1}, \\ I_{NaCa} &= I_{NaCa}^{max} [e^{\gamma\phi/RT} C_{Na}^3 C_{Ca0} - e^{(\gamma-1)\phi/RT} C_{Na0}^3 C_{Ca} \gamma_{NaCa}] \\ &\quad \times \left[ \frac{C_{NaCa}^3 + C_{Na0}^3}{C_{CaNa} + C_{Ca0}} \left[ 1 + k_{NaCa}^{sat} e^{(\gamma-1)\phi/RT} \right] \right]^{-1}, \end{aligned} \quad (22)$$

where the scaling factors are the maximum fast sodium conductance  $C_{Na}^{\max} = 14.838$  nS/pF, the maximum background sodium conductance  $C_{bNa}^{\max} = 0.00029$  nS/pF, the maximum sodium potassium pump current  $I_{NaK}^{\max} = 1.362$  pA/pF, and the maximum sodium calcium exchanger current  $I_{NaCa}^{\max} = 1000$  pA/pF, respectively. The rapid upstroke in the membrane potential is generated by the fast sodium current  $I_{Na}$  which is characterized through a three-gate formulation of Beeler–Reuter type [4] in terms of the sodium activation gate  $g_m$ , the fast sodium inactivation gate  $g_h$ , and the slow sodium inactivation gate  $g_j$ . Their evolution is governed by classical Hodgkin–Huxley type Eq. (4) of the format  $\dot{g}_{gate} = [g_{gate}^{\infty} - g_{gate}] / \tau_{gate}$  where  $g_{gate}^{\infty}$  characterizes the steady state value and  $\tau_{gate}$  denotes the time constant associated with reaching the steady state. For the sodium activation gate  $\dot{g}_m = [g_m^{\infty} - g_m] / \tau_m$ , which initiates the rapid upstroke, they take the following explicit representations.

$$\begin{aligned} g_m^{\infty} &= [1 + e^{(-56.86 - \phi)/9.03}]^{-2}, \\ \tau_m &= 0.1[1 + e^{(-60 - \phi)/5}]^{-1} [[1 + e^{(\phi + 35)/5}]^{-1} + [1 + e^{(\phi - 50)/200}]^{-1}]. \end{aligned} \quad (23)$$

The kinetics of inactivation are exponential. For the fast sodium inactivation gate  $\dot{g}_h = [g_h^{\infty} - g_h] / \tau_h$ , which initiates a fast inactivation of the sodium channel almost instantaneously after the rapid upstroke, the steady state value and the corresponding time constant can be expressed as follows.

$$\begin{aligned} g_h^{\infty} &= [1 + e^{(\phi + 71.55)/7.43}]^{-2}, \\ \tau_h &= \begin{cases} 0.1688[1 + e^{-(\phi + 10.66)/11.1}] & \text{if } \phi \geq -40, \\ [0.057e^{-(\phi + 80)/6.8} + 2.7e^{0.079\phi} + 3.1 \cdot 10^5 e^{0.3485\phi}]^{-1} & \text{if } \phi < -40. \end{cases} \end{aligned} \quad (24)$$

For the slow sodium inactivation gate  $\dot{g}_j = [g_j^{\infty} - g_j] / \tau_j$ , which gradually inactivates the fast sodium channel over a time span of 100–200 ms, these constants take the following form.

$$\begin{aligned} g_j^{\infty} &= [1 + e^{(\phi + 71.55)/7.43}]^{-2}, \\ \tau_j &= [\alpha_j + \beta_j]^{-1}, \\ \alpha_j &= \begin{cases} 0 & \text{if } \phi \geq -40, \\ [-2.5428 \cdot 10^4 e^{0.2444\phi} - 6.948 \cdot 10^{-6} e^{-0.04391\phi}] & \text{if } \phi < -40 \\ [\phi + 37.78][1 + e^{0.311(\phi + 79.23)}]^{-1} & \end{cases} \\ \beta_j &= \begin{cases} 0.6e^{0.057\phi}[1 + e^{-0.1(\phi + 32)}]^{-1} & \text{if } \phi \geq -40, \\ [0.02424e^{-0.01052\phi}[1 + e^{-0.1378(\phi + 40.14)}]^{-1}] & \text{if } \phi < -40. \end{cases} \end{aligned} \quad (25)$$

The sodium ions that entered the cell rapidly during the fast upstroke are removed from the cell by the sodium potassium pump  $I_{NaK}$ , a metabolic pump that continuously expels sodium ions from the cell interior and pumps in potassium ions. The intracellular sodium concentration is further affected by expulsion of intracellular calcium ions through sodium calcium exchange  $I_{NaCa}$ . The additional parameters for the sodium potassium pump current  $I_{NaK}$  and for the sodium calcium exchanger current  $I_{NaCa}$  are the extracellular sodium, potassium, and calcium concentrations  $c_{Na0} = 140$  mM,  $c_{K0} = 5.4$  mM, and  $c_{Ca0} = 2$  mM, the half saturation constants  $c_{Ca-Na} = 1.38$  mM,  $c_{NaCa} = 87.5$  mM,  $c_{KNa} = 1$  mM,  $c_{NaK} = 40$  mM, the sodium calcium saturation factor  $k_{NaCa}^{\text{sat}} = 0.1$ , the outward sodium calcium pump current enhancing factor  $\gamma_{NaCa} = 2.5$ , and the voltage dependent sodium calcium parameter  $\gamma = 0.35$ .

## 4.2. Specification of potassium concentration, currents, and gating variables

Potassium plays an important role in maintaining the appropriate action potential profile in all four phases after the rapid upstroke. At rest, the intracellular potassium concentration is typically about  $c_K = 138.3$  mM, and the related equilibrium potential would be  $\phi_K = -86.6$  mV according to Eq. (19). This value is very close to, but slightly more negative than, the resting potential of  $\phi = -86$  mV actually measured in ventricular cardiomyocytes. Unlike for sodium, the electrical force that pulls potassium ions inward is slightly weaker than the chemical force of diffusion pulling potassium ions outward. Accordingly, potassium tends to leave the resting cell. At the end of the rapid upstroke, before the beginning of the plateau, we can observe an early, brief period of limited repolarization governed by the voltage-activated transient outward current  $I_{t0}$ . During the following plateau phase, we observe an influx of calcium ions which is balanced by the efflux of an equal amount of positively charged potassium ions, mainly regulated by the rapid and slow delayed rectifier currents  $I_{Kr}$  and  $I_{Ks}$ . The final repolarization phase can almost exclusively be attributed to potassium ions leaving the cell such that the membrane potential can return to its resting state, see Fig. 2. In summary, the evolution of the potassium concentration

$$\dot{c}_K = -\frac{C}{VF} [I_{K1} + I_{Kr} + I_{Ks} - 2I_{NaK} + I_{pK} + I_{t0} + I_{stim}] \quad (26)$$

is mainly controlled by four currents, the inward rectifier current  $I_{K1}$ , the rapid delayed rectifier current  $I_{Kr}$ , the slow delayed rectifier current  $I_{Ks}$ , and the transient outward current  $I_{t0}$ . Moreover, it is affected by the sodium potassium pump current  $I_{NaK}$ , the plateau potassium current  $I_{pK}$ , and the external stimulus current  $I_{stim}$ . Currents are scaled by the membrane capacitance per unit surface area  $C = 185$  pF, the cytoplasmic volume  $V = 16,404 \mu\text{m}^3$ , and the Faraday constant  $F = 96.4867$  C/mmol. The individual potassium related currents are defined as follows,

$$\begin{aligned} I_{K1} &= C_{K1}^{\max} g_{K1}^{\infty} [c_{K0}/5.4]^{1/2} [\phi - \phi_K], \\ I_{Kr} &= C_{Kr}^{\max} g_{Kr1} g_{Kr2} [c_{K0}/5.4]^{1/2} [\phi - \phi_K], \\ I_{Ks} &= C_{Ks}^{\max} g_{Ks}^2 [\phi - \phi_K], \\ I_{NaK} &= I_{NaK}^{\max} [c_{K0} c_{Na}] [c_{Na} + c_{NaK}] [c_{K0} + c_{KNa}] \\ &\quad \times [1 + 0.1245e^{-0.1\phi/RT} + 0.0353e^{-\phi/RT}]^{-1}, \\ I_{pK} &= C_{pK}^{\max} [1 + e^{(25 - \phi)/5.98}]^{-1} [\phi - \phi_K], \\ I_{t0} &= C_{t0}^{\max} g_t g_s [\phi - \phi_K], \end{aligned} \quad (27)$$

where the individual scaling factors are the maximum inward rectifier conductance  $C_{K1}^{\max} = 5.405$  nS/pF, the maximum rapid delayed rectifier conductance  $C_{Kr}^{\max} = 0.096$  nS/pF, the maximum slow delayed rectifier conductance for epicardial and endocardial cells  $C_{Ks,epi}^{\max} = C_{Ks,endo}^{\max} = 0.245$  nS/pF and for M cells  $C_{Ks,M}^{\max} = 0.062$  nS/pF, the maximum sodium potassium pump current  $I_{NaK}^{\max} = 1.362$  pA/pF, the maximum potassium pump conductance  $C_{pK}^{\max} = 0.0146$  nS/pF, and the maximum transient outward conductance for epicardial and M cells  $C_{t0,epi}^{\max} = C_{t0,M}^{\max} = 0.294$  nS/pF and for endocardial cells  $C_{t0,endo}^{\max} = 0.073$  nS/pF. The maximum inward rectifier current  $I_{K1}$ , which is most active during the later phases of the action potential, depends explicitly on the extracellular potassium concentration  $c_{K0} = 5.4$  mM. It is further characterized through the time-independent inward rectification factor  $g_{K1}^{\infty}$  parameterized in terms of the potential equilibrium potential  $\phi_K$  given in Eq. (19).

$$g_{K1}^{\infty} = \alpha_{K1} [\alpha_{K1} + \beta_{K1}]^{-1}$$

with

$$\alpha_{K1} = 0.1 [1 + e^{0.06(\phi - \phi_K - 200)}]^{-1}, \quad (28)$$

$$\beta_{K1} = [3e^{0.0002(\phi - \phi_K + 100)} + e^{0.1(\phi - \phi_K - 10)}] [1 + e^{-0.5(\phi - \phi_K)}]^{-1}.$$

The action potential plateau is characterized through the influx of charged calcium ions balanced by the efflux of potassium ions. The latter is basically governed by the rapid and slow delayed rectifier current  $I_{Kr}$  and  $I_{Ks}$ . The channel for the rapid delayed rectifier current  $I_{Kr}$  is gated by an activation gate  $\dot{g}_{x1} = [g_{x1}^{\infty} - g_{x1}] / \tau_{x1}$  with the steady state value and time constant given as

$$g_{xr1}^{\infty} = [1 + e^{(-26 - \phi)/7}]^{-1}, \quad (29)$$

$$\tau_{xr1} = 2700 [1 + e^{(-45 - \phi)/10}]^{-1} [1 + e^{(\phi + 30)/11.5}]^{-1}$$

and by an inactivation gate  $\dot{g}_{x2} = [g_{x2}^{\infty} - g_{x2}] / \tau_{x2}$ , with the following steady state value and time constant.

$$g_{xr2}^{\infty} = [1 + e^{(\phi + 88)/24}]^{-1}, \quad (30)$$

$$\tau_{xr2} = 3.36 [1 + e^{(-60 - \phi)/20}]^{-1} [1 + e^{(\phi - 60)/20}]^{-1}.$$

The channel for the slow delayed rectifier current  $I_{Ks}$  is a function of the reversal potential  $\phi_{Ks} = RT/F \log[(c_{K0} + p_{KNa} c_{Na0}) / (c_K + p_{KNa} c_{Na})]^{-1}$  parameterized in terms of its permeability to sodium ions  $p_{KNa} = 0.03$ . It is gated by an activation gate  $\dot{g}_{xs} = [g_{xs}^{\infty} - g_{xs}] / \tau_{xs}$  in terms of the following parameterization.

$$g_{xs}^{\infty} = [1 + e^{(-5 - \phi)/14}]^{-1}, \quad (31)$$

$$\tau_{xs} = 1100 [1 + e^{(-10 - \phi)/6}]^{-1/2} [1 + e^{(\phi - 60)/20}]^{-1}.$$

The transient potassium outward current  $I_{t0}$  is responsible for the transition between the rapid upstroke and the plateau phase, where it generates an early short period of limited repolarization. It is gated by a voltage-dependent activation gate  $g_r$  with  $\dot{g}_r = [g_r^{\infty} - g_r] / \tau_r$  defined through the following steady state value and time constant,

$$g_r^{\infty} = [1 + e^{(20 - \phi)/6}]^{-1}, \quad (32)$$

$$\tau_r = 9.5 e^{-(\phi + 40)^2 / 1800} + 0.8$$

and by the voltage-dependent inactivation gate  $g_s$  with  $\dot{g}_s = [g_s^{\infty} - g_s] / \tau_s$  with the steady state value and time constant given as follows.

$$\left. \begin{aligned} g_s^{\infty} &= [1 + e^{(\phi + 20)/5}], \\ \tau_s &= 85 e^{-(\phi + 45)^2 / 320} + 5 [1 + e^{(\phi - 20)/5}] + 3, \end{aligned} \right\} \text{epicardium} \quad (33)$$

$$\left. \begin{aligned} g_s^{\infty} &= [1 + e^{(\phi + 28)/5}], \\ \tau_s &= 1000 e^{-(\phi + 67)^2 / 1000} + 8, \end{aligned} \right\} \text{endocardium}.$$

This voltage dependent potassium inactivation gate displays a significantly different behavior for epicardial and endocardial cells and is therefore characterized differently for the individual cell types. Similar to the previous subsection, we have introduced the extracellular sodium and potassium concentrations  $c_{Na0} = 140$  mM and  $c_{K0} = 5.4$  mM, and the half saturation constants  $c_{KNa} = 1$  mM and  $c_{NaK} = 40$  mM.

#### 4.3. Specification of calcium concentration, currents, and gating variables

Calcium is the key player to translate electrical excitation into mechanical contraction. With a typical intracellular resting con-

centrations of  $c_{Ca} = 0.08$   $\mu$ M, its equilibrium potential of  $\phi_{Ca} = +135.3$  mV is much larger than the resting potential. During the plateau of the action potential, calcium ions enter the cell through calcium channels that typically activate and inactivate much more slowly than the fast sodium channels. The influx of positively charged calcium ions through the L-type calcium channel  $I_{CaL}$  is balanced by an efflux of positively charged potassium ions. The letter  $L$  is meant to indicate the long lasting nature of the inward calcium current. Overall, changes in the intracellular calcium concentration

$$\dot{c}_{Ca} = \gamma_{Ca} \left[ -\frac{C}{2VF} [I_{CaL} + I_{bCa} + I_{pCa} - 2I_{NaCa}] + I_{leak} - I_{up} + I_{rel} \right] \quad (34)$$

are affected by the L-type calcium current  $I_{CaL}$ , the background calcium current  $I_{bCa}$ , the plateau calcium current  $I_{pCa}$ , and the sodium calcium pump current  $I_{NaCa}$ , weighted by the membrane capacitance per unit surface area  $C = 185$  pF, the cytoplasmic volume  $V = 16,404$   $\mu$ m<sup>3</sup>, and the Faraday constant  $F = 96,4867$  C/mmol. In addition, the intracellular calcium concentration is affected by a calcium loss to the sarcoplasmic reticulum characterized through the leakage current  $I_{leak}$ , the sarcoplasmic reticulum uptake current  $I_{up}$ , and the sarcoplasmic reticulum release current  $I_{rel}$ . The individual calcium related currents are defined as follows,

$$\begin{aligned} I_{CaL} &= C_{CaL}^{\max} g_d g_r g_{rCa} [4\phi F^2] / [RT] [c_{Ca} e^{2\phi F / RT} - 0.341 c_{Ca0}] [e^{2\phi F / RT} - 1]^{-1}, \\ I_{bCa} &= C_{bCa}^{\max} [\phi - \phi_{Ca}], \\ I_{pCa} &= C_{pCa}^{\max} c_{Ca} [c_{pCa} + c_{Ca}]^{-1}, \\ I_{NaCa} &= J_{NaCa}^{\max} [e^{\gamma \phi F / RT} c_{Na}^3 c_{Ca0} - e^{(\gamma - 1)\phi F / RT} c_{Na0}^3 c_{Ca} \gamma_{NaCa}] \\ &\quad \times [c_{NaCa}^3 + c_{Na0}^3] [c_{CaNa} + c_{Ca0}] [1 + k_{NaCa}^{\text{sat}} e^{(\gamma - 1)\phi F / RT}]^{-1}, \\ I_{leak} &= J_{leak}^{\max} [c_{Ca}^{\text{sr}} - c_{Ca}], \\ I_{up} &= J_{up}^{\max} [1 + c_{up}^2 / c_{Ca}^2]^{-1}, \\ I_{rel} &= J_{rel}^{\max} g_d g_g [1 + \gamma_{rel} c_{Ca}^{\text{sr}2} (c_{rel}^2 + c_{Ca}^{\text{sr}2})^{-1}], \end{aligned} \quad (35)$$

where the individual scaling factors are the maximum calcium conductance  $C_{CaL}^{\max} = 0.175$  mm<sup>3</sup>  $\mu$ F<sup>-1</sup> s<sup>-1</sup>, the maximum background calcium conductance  $C_{bCa}^{\max} = 0.000592$  nS/pF, the maximum plateau calcium conductance  $C_{pCa}^{\max} = 0.825$  nS/pF, the maximum sodium calcium pump current  $J_{NaCa}^{\max} = 1000$  pA/pF, the maximum leakage current  $J_{leak}^{\max} = 0.08$  s<sup>-1</sup>, the maximum sarcoplasmic reticulum calcium uptake current  $J_{up}^{\max} = 0.000425$  mM/ms, and the maximum sarcoplasmic reticulum calcium release current  $J_{rel}^{\max} = 8.232$  mM/s. The major calcium channel, the long-lasting L-type calcium channel  $I_{CaL}$ , is controlled by the voltage-dependent activation gate  $\dot{g}_d = [g_d^{\infty} - g_d] / \tau_g$  characterized through the following steady state value and time constant

$$g_d^{\infty} = [1 + e^{(-5 - \phi)/7.5}]^{-1},$$

$$\tau_d = [1.4 [1 + e^{(-35 - \phi)/13}]^{-1} + 0.25] [1.4 [1 + e^{(\phi + 5)/5}] + [1 + e^{(50 - \phi)/20}]]^{-1}, \quad (36)$$

by the voltage-dependent inactivate gate  $\dot{g}_r = [g_r^{\infty} - g_r] / \tau_r$  characterized through

$$g_r^{\infty} = [1 + e^{(\phi + 20)/7}]^{-1}, \quad (37)$$

$$\tau_r = 1125 e^{-(\phi + 27)^2 / 240} + 165 [1 + e^{(25 - \phi)/10}]^{-1} + 80$$

and by the intracellular calcium dependent inactivation gate  $\dot{g}_{rCa} = [g_{rCa}^{\infty} - g_{rCa}] / \tau_{rCa}$  characterized through

$$g_{fCa}^{\infty} = 0.685 \left[ \left[ 1 + (c_{Ca}/0.000325)^8 \right]^{-1} + 0.1 \left[ 1 + e^{(c_{Ca}-0.0005)/0.0001} \right]^{-1} + 0.2 \left[ 1 + e^{(c_{Ca}-0.00075)/0.0008} \right]^{-1} + 0.23 \right],$$

$$\tau_{fCa} = \begin{cases} \infty & \text{if } g_{fCa}^{\infty} > g_{fCa} \text{ and } \phi \geq -60 \text{ mV,} \\ 2 \text{ ms} & \text{otherwise.} \end{cases} \quad (38)$$

Accordingly, the steady state response  $g_{fCa}^{\infty}$  has a switchlike shape when going from no inactivation to considerable but incomplete inactivation, depending mildly on the calcium concentration  $c_{Ca}$  for suprathreshold concentrations. Last, the calcium-induced calcium release current  $I_{rel}$  is characterized through the activation gate  $g_d$ , the same gate that is also activating the L-type calcium channel of  $I_{CaL}$ , and through the calcium-dependent inactivation gate  $\dot{g}_g = [g_g^{\infty} - g_g]/\tau_g$  characterized through the following steady state value and time constant.

$$g_g^{\infty} = \begin{cases} [1 + c_{Ca}^6/0.00035^6]^{-1} & \text{if } c_{Ca} \leq 0.00035, \\ [1 + c_{Ca}^{16}/0.00035^{16}]^{-1} & \text{otherwise,} \end{cases} \quad (39)$$

$$\tau_g = \begin{cases} \infty & \text{if } g_g^{\infty} > g_g \text{ and } \phi \geq -60 \text{ mV,} \\ 2 \text{ ms} & \text{otherwise.} \end{cases}$$

The remaining parameters governing the response of the plateau calcium current  $I_{pCa}$ , the calcium uptake current  $I_{up}$ , and the sarcoplasmic reticulum calcium release current  $I_{rel}$  are the half saturation constants for the plateau calcium concentration  $c_{pCa} = 0.0005$  mM, for the sarcoplasmic reticulum calcium uptake  $c_{up} = 0.00025$  mM, and for the sarcoplasmic reticulum calcium release  $c_{rel} = 0.25$  mM, respectively. The parameter  $\gamma_{NaCa} = 2.5$  has been introduced to enhance the outward nature of the sodium calcium pump current  $I_{NaCa}$ . The additional parameter  $\gamma_{rel} = 2$  weighs the relative influence of the sarcoplasmic reticulum calcium concentration on sarcoplasmic reticulum calcium release  $I_{rel}$ . Finally, we need to take into account that the total intracellular calcium concentration  $c_{Ca}^{tot} = c_{Ca} + c_{Ca}^{buf}$  in the cytoplasm is the sum of the free intracellular calcium concentration  $c_{Ca}$  and the buffered calcium concentration  $c_{Ca}^{buf} = [c_{Ca}c_{Ca}^{tot}][c_{Ca} - c_{Ca}^{buf}]^{-1}$ . The definition of the free intracellular calcium concentration in Eq. (34) is therefore weighted by the parameter  $\gamma_{Ca} = [1 + [c_{tot}c_{buf}][c_{Ca} + c_{buf}]^{-2}]^{-1}$ , where  $c_{tot} = 0.15$  mM and  $c_{buf} = 0.001$  mM are the total and half saturation cytoplasmic calcium buffer concentrations, respectively.

#### 4.4. Specification of sarcoplasmic reticulum calcium concentration, currents, and gating variables

The specification of the sarcoplasmic reticulum calcium concentration

$$\dot{c}_{Ca}^{sr} = \gamma_{Ca}^{sr} \frac{V}{V^{sr}} [-I_{leak} + I_{up} - I_{rel}] \quad (40)$$

is now relatively straightforward since it mimics the corresponding loss of intracellular calcium characterized however, now scaled by the ratio between the volume of the cytoplasm  $V = 16,404 \mu\text{m}^3$  and the volume of the sarcoplasmic reticulum  $V^{sr} = 1094 \mu\text{m}^3$ . The leakage current  $I_{leak}$ , the sarcoplasmic reticulum uptake current  $I_{up}$ , and the sarcoplasmic reticulum release current  $I_{rel}$  are defined as before.

$$I_{leak} = I_{leak}^{max} [c_{Ca}^{sr} - c_{Ca}],$$

$$I_{up} = I_{up}^{max} \left[ 1 + c_{up}^2/c_{Ca}^2 \right]^{-1}, \quad (41)$$

$$I_{rel} = I_{rel}^{max} g_d g_g \left[ 1 + \gamma_{rel} c_{Ca}^{sr2} [c_{rel} + c_{Ca}^{sr2}]^{-1} \right].$$

The maximum leakage current  $I_{leak}^{max} = 0.08 \text{ s}^{-1}$ , the maximum sarcoplasmic reticulum calcium uptake current  $I_{up}^{max} = 0.000425 \text{ mM/ms}$ ,

and the maximum sarcoplasmic reticulum calcium release current  $I_{rel}^{max} = 8.232 \text{ mM/s}$ , the half saturation constants for the calcium uptake  $c_{up} = 0.00025 \text{ mM}$ , and for the calcium release  $c_{rel} = 0.25 \text{ mM}$ , and the weighting coefficient  $\gamma_{rel} = 2$  have already been introduced in the previous subsection. Similar to the previous subsection, we need to take into account that the total calcium concentration in the sarcoplasmic reticulum  $c_{Ca}^{sr,tot} = c_{Ca}^{sr} + c_{Ca}^{sr,buf}$  is the sum of the free sarcoplasmic reticulum calcium concentration  $c_{Ca}^{sr}$  and the buffered sarcoplasmic reticulum calcium concentration  $c_{Ca}^{sr,buf} = [c_{Ca}^{sr}c_{Ca}^{sr,tot}][c_{Ca}^{sr} - c_{Ca}^{sr,buf}]^{-1}$ . The definition of the free sarcoplasmic reticulum calcium concentration in Eq. (40) is therefore weighted by the parameter  $\gamma_{Ca}^{sr} = [1 + [c_{tot}^{sr}c_{buf}^{sr}][c_{Ca}^{sr} + c_{Ca}^{sr,buf}]^{-2}]^{-1}$ , where  $c_{tot}^{sr} = 10 \text{ mM}$  and  $c_{buf}^{sr} = 0.3 \text{ mM}$  are the total and half saturation sarcoplasmic reticulum calcium buffer concentrations, respectively.

#### 5. Discrete model problem for human ventricular cardiomyocytes

Finally, we can specify the discrete ion concentration residuals  $R_{ion}$  introduced in Eq. (14). For our particular model problem of human ventricular cardiomyocytes we use the individual righthand sides  $f_{ion}^c$  defined in Eqs. (26), (21), (34), and (40).

$$R_K^c = c_K - c_K^n + \frac{C}{VF} [I_{K1} + I_{Kr} + I_{Ks} - 2I_{NaK} + I_{pK} + I_{t0} + I_{stim}] \Delta t \doteq 0,$$

$$R_{Na}^c = c_{Na} - c_{Na}^n + \frac{C}{VF} [I_{Na} + I_{bNa} + 3I_{NaK} + 3I_{NaCa}] \Delta t \doteq 0,$$

$$R_{Ca}^c = c_{Ca} - c_{Ca}^n + \frac{C}{2VF} [I_{CaL} + I_{bCa} + I_{pCa} - 2I_{NaCa}] - I_{leak} + I_{up} - I_{rel} \gamma_{Ca} \Delta t \doteq 0,$$

$$R_{Ca}^{sr,c} = c_{Ca}^{sr} - c_{Ca}^{sr,n} + \frac{V}{V^{sr}} [I_{leak} - I_{up} + I_{rel}] \gamma_{Ca}^{sr} \Delta t \doteq 0. \quad (42)$$

Note that for our algorithmic formulation, we have re-arranged the vector of residuals  $R_{ion}^c = [R_K^c, R_{Na}^c, R_{Ca}^c, R_{Ca}^{sr,c}]$  and the vector of ion concentrations  $c_{ion} = [c_K, c_{Na}, c_{Ca}, c_{Ca}^{sr}]$  to obtain a conveniently sparse iteration matrix  $K_{ion}^c$ . According to Eq. (15), this iteration matrix for the local Newton iteration is derived as the linearization of the residual vector  $R_{ion}^c$  with respect to the vector of ion concentrations  $c_{ion}$ .

$$K_{ion}^c = d_{c_{ion}} R_{ion}^c = \begin{bmatrix} d_{c_K} R_K^c & d_{c_{Na}} R_K^c & 0 & 0 \\ 0 & d_{c_{Na}} R_{Na}^c & d_{c_{Ca}} R_{Na}^c & 0 \\ 0 & d_{c_{Na}} R_{Ca}^c & d_{c_{Ca}} R_{Ca}^c & d_{c_{Ca}} R_{Ca}^{sr,c} \\ 0 & 0 & d_{c_{Ca}} R_{Ca}^{sr,c} & d_{c_{Ca}} R_{Ca}^{sr,c} \end{bmatrix}. \quad (43)$$

At convergence, i.e., at chemical equilibrium, we can finally calculate the source term  $f^b(\phi, g_{gate}, c_{ion})$  of the electrical problem (10) according to Eq. (20).

$$f^b = -[I_{Na} + I_{bNa} + I_{NaK} + I_{NaCa} + I_{K1} + I_{Kr} + I_{Ks} + I_{pK} + I_{t0} + I_{CaL} + I_{bCa} + I_{pCa}]. \quad (44)$$

Its linearization  $d_{\phi} f^b$  with respect to the membrane potential  $\phi$

$$d_{\phi} f^b = -[d_{\phi} I_{Na} + d_{\phi} I_{bNa} + d_{\phi} I_{NaK} + d_{\phi} I_{NaCa} + d_{\phi} I_{K1} + d_{\phi} I_{Kr} + d_{\phi} I_{Ks} + d_{\phi} I_{pK} + d_{\phi} I_{t0} + d_{\phi} I_{CaL} + d_{\phi} I_{bCa} + d_{\phi} I_{pCa}], \quad (45)$$

then enters the iteration matrix for the global Newton iteration (11) to ensure optimal quadratic convergence in the proximity of the solution  $\phi$ . The linearizations introduced in Eqs. (43) and (45) are elaborated in detail in Appendix A.

## 6. Examples

### 6.1. Electrochemistry in a human ventricular cardiomyocyte

To simulate electrochemical coupling in a single epicardial human ventricular cardiomyocyte, we apply the local version of the algorithm described in Table 1, ignoring the divergence term of Eq. (7) that has been introduced to model global tissue conductivity. Accordingly, our implementation of the discrete ventricular cell model uses an outer global Newton iteration to solve for the membrane potential  $\phi$  and an inner local Newton iteration to calculate the ion concentrations  $c_{ion}$  and the gating variables  $g_{gate}$ . We initialize the global membrane potential,  $\phi = -86$  mV, and the local ion concentrations,  $c_{Na} = 11.6$  mM,  $c_K = 138.3$  mM, and  $c_{Ca} = 0.08$   $\mu$ M, mimicking the resting state. For the gating variables, we choose the following initial conditions  $g_m = 0$ ,  $g_h = 0.75$ ,  $g_j = 0.75$ ,  $g_d = 0$ ,  $g_r = 1$ ,  $g_{rCa} = 1$ ,  $g_s = 0$ ,  $g_{xs} = 1$ ,  $g_{xr1} = 0$ ,  $g_{xr2} = 0$ ,  $g_{xK1\infty} = 0.05$ , and  $g_g = 1$ . Figs. 3–6 represent the electrochemical characteristics for the human ventricular epicardial cardiomyocyte, using the material parameters summarized in Table 2, an initial electrical stimulus above the critical threshold, and a discrete time step of  $\Delta t = 0.02$  ms, to match the time step used in the original publication [58]. We have been able to demonstrate though that the time step size could easily be increased by a factor ten without any substantial loss of accuracy. To validate our algorithm against the explicit finite difference results reported in the literature, we reproduce the steady-state profiles  $g_{gate}^{\infty}$  and the time constant profiles  $\tau_{gate}$  plotted against the membrane potential  $\phi$ . Fig. 3 shows the resulting curves for the individual gating variables. Note that the discontinuities in the time constants of  $\tau_h$  and  $\tau_j$  which are reported in Fig. 3c and e are handled in a piece-wise manner with the partial derivatives and sensitivities calculated for the given membrane potential range. As expected, the steady-state values and time constants coincide perfectly with graphs reported in the original model based on an explicit time integration scheme [58].

Fig. 4 illustrates the temporal evolution of all thirteen gating variables  $g_{gate}$  throughout the duration of a typical action potential. The collection of gating variable profiles nicely illustrates the time sequence of activation and inactivation of the individual ion channels. It also documents which of the gates are slow and fast responding. Fig. 4a–c document the activation, the fast inactivation, and the slow inactivation gates  $g_m$ ,  $g_h$ , and  $g_j$  for the fast sodium current  $I_{Na}$  that governs the rapid upstroke of the action potential  $\phi$ . It is obvious that the inactivation gates  $g_h$  and  $g_j$  open slightly after the activation gate  $g_m$  is closed, with the fast gate  $g_h$  responding more rapidly than the slow gate  $g_j$ . Fig. 4d–f show the activation, the voltage-dependent inactivation, and the intracellular calcium dependent inactivation gates  $g_d$ ,  $g_r$ , and  $g_{rCa}$  for the L-type calcium current  $I_{CaL}$  that is activated during the action potential upstroke. It is obvious that the long lasting nature of the L-type calcium current can be attributed to the slow response profiles of  $g_d$  and  $g_r$ . Fig. 4g and h illustrate the transient outward channel's activation and inactivation gates  $g_s$  and  $g_{s1}$ , which manifest themselves in a sharp initial peak in the transient outward current  $I_{to}$  that initiates the short period of early repolarization after initial excitation. Fig. 4i–l illustrate the slow delayed rectifier gate  $g_{xs}$ , the rapid delayed rectifier activation and inactivation gates  $g_{xr1}$  and  $g_{xr2}$ , and the inward rectification factor  $g_{xK1}^{\infty}$  which collectively determine the potassium concentration profile during the plateau and repolarization phases. Fig. 4m displays the calcium dependent inactivation gate of the sarcoplasmic reticulum release current  $I_{rel}$  that characterizes intracellular calcium dynamics through a sharp rapid inactivation towards the end of the repolarization phase.

The evolution of the ionic currents  $I_{crit}$  over an excitation cycle is shown in Fig. 5. The current profiles nicely capture the basic char-

acteristic features of human ventricular cardiomyocytes. The dominance of the fast sodium current  $I_{Na}$  in Fig. 5a, the transient outward current  $I_{to}$  in Fig. 5i, and the L-type calcium current  $I_{CaL}$  in Fig. 5j is clearly evident. This implies that the sodium, potassium, and calcium concentration profiles primarily depend on these three channels. During the rapid depolarization phase of the cardiomyocyte, we observe a rapid activity of the fast sodium channel  $I_{Na}$ . During the following period of partial repolarization, the transient outward current  $I_{to}$  is responsible for a sharp efflux of potassium ions generating the familiar notch in the action potential profile shown in Fig. 1. The L-type calcium current  $I_{CaL}$  is activated rapidly during the depolarization phase and inactivated slowly during the following phases. It is important to note that this calcium current  $I_{CaL}$  displays a discontinuity at  $\phi$  equal to zero. Since we need to determine its sensitivities and partial derivatives to guarantee optimal quadratic convergence of our Newton Raphson algorithm, we apply L'Hospital's rule to calculate the algorithmic derivatives in the proximity of this singularity. Altogether, the results in Fig. 5 correlate well with the reported currents calculated with the explicit time integration scheme reported in the original manuscript [58]. Recall that the ionic current profiles directly feed back into the action potential itself as illustrated in Fig. 2 and discussed in detail in the introduction.

Lastly, Fig. 6 documents the evolution of the four ion concentrations throughout a typical action potential cycle. As indicative of the three major currents, i.e., the fast sodium current  $I_{Na}$ , the transient outward current  $I_{to}$ , and the L-type calcium current  $I_{CaL}$ , the effluxes and influxes directly impact the corresponding ion concentration profiles. The sodium concentration  $c_{Na}$  shown in Fig. 6a is primarily affected by the fast sodium current  $I_{Na}$  initiating a fast intracellular sodium increase to create the rapid upstroke of the action potential. It then decays slowly towards the end of the repolarization phase and increases gradually during the resting phase. These continuous gradual changes are primarily caused by the sodium potassium pump  $I_{NaK}$  and by the sodium calcium exchanger  $I_{NaCa}$ . The potassium concentration  $c_K$  displayed in Fig. 6b decreases in a somewhat stepwise fashion regulated by the sequential activation of the transient outward current  $I_{to}$ , the inward rectifier current  $I_{K1}$ , and the rapid and slow delayed rectifier currents  $I_{Kr}$  and  $I_{Ks}$ . At the end of the repolarization phase, we can observe a gradual smooth increase to bring the potassium concentration back to its original value. The calcium concentration  $c_{Ca}$  shown in Fig. 6c increases rapidly through the opening L-type calcium channel  $I_{CaL}$  which is activated slightly after the action potential upstroke. After this sharp increase, the calcium concentration decays smoothly to its original value throughout the remaining phases of the action potential. The intracellular calcium concentration  $c_{Ca}$  matches extremely well with the explicit finite difference result [58]. Its profile obviously impacts the intracellular calcium dynamics, and directly affects the calcium concentration in the sarcoplasmic reticulum  $c_{Ca}^{sr}$  shown in Fig. 5d. In summary, the model reproduces the classical characteristics of an initial increase in the sodium concentration followed by an increase in calcium and a decrease in potassium, jointly generating the characteristic plateau. In this model, sodium then experiences a decrease, a minimum, and a gradual increase paired with a potassium increase. Note that despite the drastic changes in the membrane potential from  $-86$  mV to  $+20$  mV illustrated in Fig. 1, the overall changes in the individual ion concentrations remain incredibly small, usually in the order of less than one percent.

### 6.2. Electrochemistry in the human heart

The final example demonstrates the potential of the proposed algorithm in a nonlinear finite element analysis of electrochemical

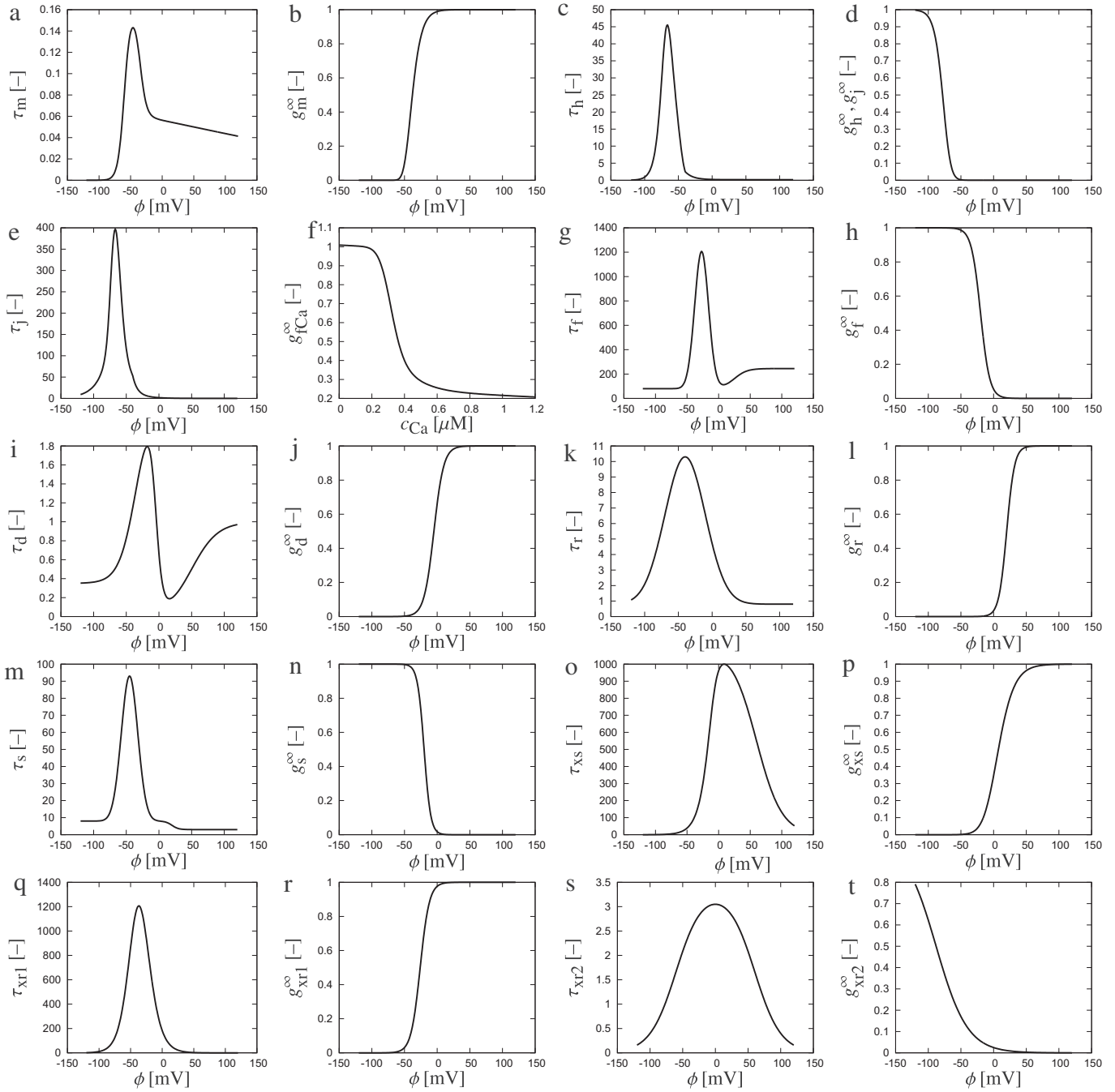


**Fig. 3.** Electrochemistry in a human ventricular cardiomyocyte. Voltage dependent evolution of time constants  $\tau_m$ ,  $\tau_h$ ,  $\tau_j$  and steady state values  $g_m^\infty$ ,  $g_h^\infty$ ,  $g_j^\infty$  for sodium activation and fast and slow sodium inactivation gates  $g_m$ ,  $g_h$ ,  $g_j$ . Calcium concentration dependent evolution of steady state value  $g_{Ca}^\infty$  for intracellular calcium dependent calcium inactivation gate  $g_{Ca}$ . Voltage dependency evolution of time constants  $\tau_d$ ,  $\tau_f$  and steady state values  $g_d^\infty$ ,  $g_f^\infty$  for L-type calcium activation and inactivation gates  $g_d$ ,  $g_f$ . Voltage dependency evolution of time constants  $\tau_r$ ,  $\tau_s$  and steady state values  $g_r^\infty$ ,  $g_s^\infty$  for transient potassium outward activation and inactivation gates  $g_r$ ,  $g_s$ . Voltage dependency evolution of time constants  $\tau_{xs}$ ,  $\tau_{xr1}$ ,  $\tau_{xr2}$  and steady state values  $g_{xs}^\infty$ ,  $g_{xr1}^\infty$ ,  $g_{xr2}^\infty$  for slow delayed rectifier gate and rapid delayed rectifier activation and inactivation gates  $g_{xs}$ ,  $g_{xr1}$ ,  $g_{xr2}$ .

coupling using a patient-specific human heart model reconstructed from magnetic resonance images [32]. A tetrahedral heart mesh of 11,347 elements and 3,129 nodes is reconstructed from MRI images. For the global membrane potential,  $\phi = -86$  mV, and the local ion concentrations,  $c_{Na} = 11.6$  mM,  $c_K = 138.3$  mM,  $c_{Ca} = 0.08$   $\mu$ M, and  $c_{Ca}^{sr} = 0.56$  mM, we apply initial conditions which mimic the resting state. For the gating variables, we choose the following initial conditions  $g_m = 0$ ,  $g_h = 0.75$ ,  $g_j = 0.75$ ,  $g_d = 0$ ,  $g_f = 1$ ,  $g_{rCa} = 1$ ,  $g_r = 0$ ,  $g_s = 1$ ,  $g_{xs} = 0$ ,  $g_{xr1} = 0$ ,  $g_{xr2} = 0$ ,  $g_{xK1\infty} = 0.05$ , and  $g_g = 1$  similar to the previous single cell example. Moreover,

we apply the common assumption of homogeneous Neumann boundary conditions. The heart is excited through the application of an external stimulus in the region of the atrioventricular node in the center of the basal septum. Following the literature, we adopt a time step size of  $\Delta t = 0.125$  ms. However, we were able to demonstrate the use of larger time steps, particularly when combined with faster conductivities. For the sake of simplicity, we select an isotropic conductivity  $D = d_{iso}I$  with  $d_{iso} = 0.5$  mm<sup>2</sup>/ms. This value is calibrated by means of global electrocardiogram profiles [32], such that the initial excitation of the heart occurs in

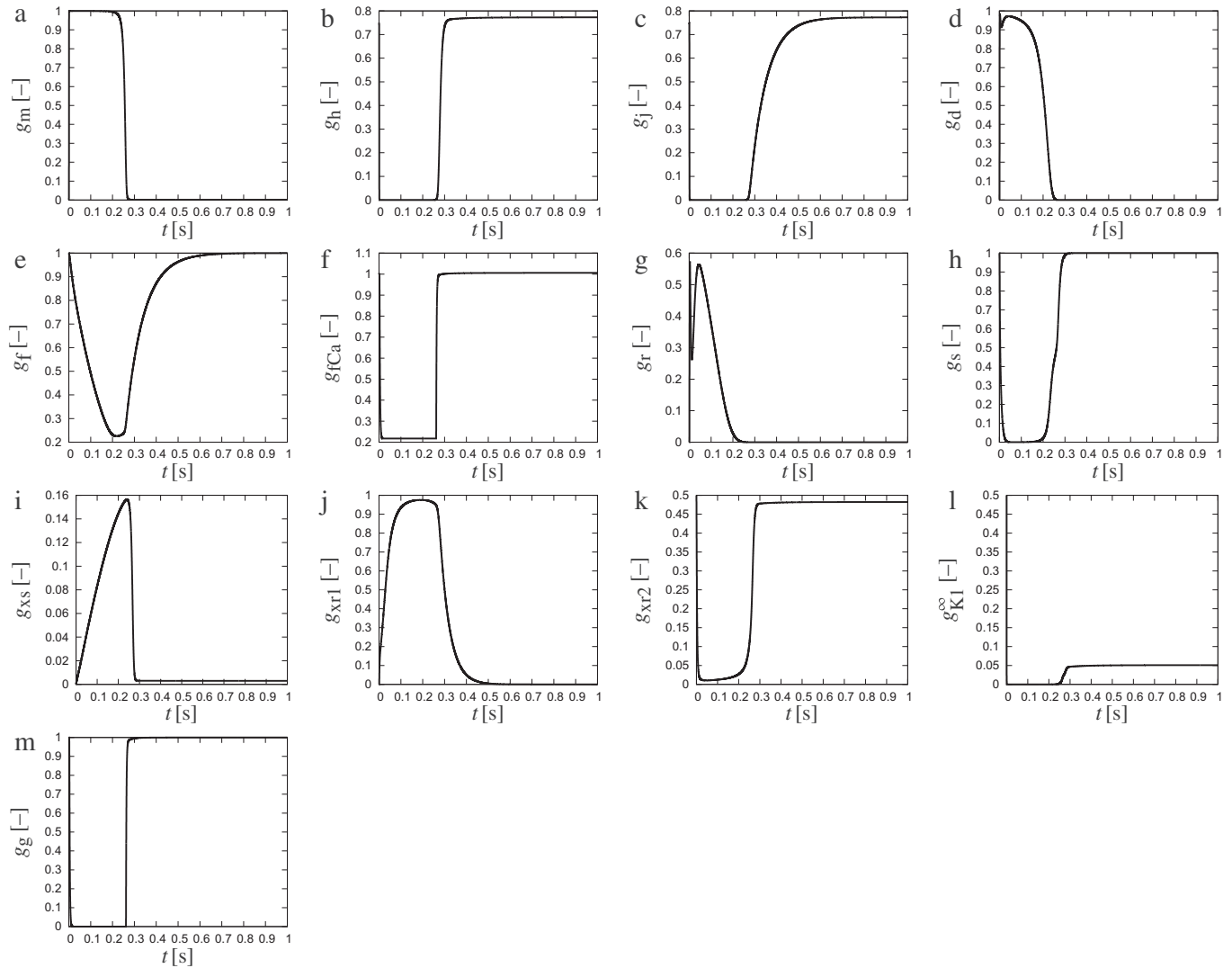


**Fig. 4.** Electrochemistry in a human ventricular cardiomyocyte. Temporal evolution of sodium activation gate  $g_m$ , fast sodium inactivation gate  $g_h$ , slow sodium inactivation gate  $g_j$ , L-type calcium activation gate  $g_d$ , L-type calcium inactivation gate  $g_f$ , intracellular calcium dependent calcium inactivation gate  $g_{fCa}$  transient outward activation gate  $g_r$ , transient outward inactivation gate  $g_s$ , slow delayed rectifier gate  $g_{xS}$ , rapid delayed rectifier activation gate  $g_{xr1}$ , rapid delayed rectifier inactivation gate  $g_{xr2}$ , inward rectification factor  $g_{K1}^\infty$ , and calcium-dependent inactivation gate  $g_g$ .

approximately 30 ms. In the future, we will enhance the model by incorporating an anisotropic conductivity  $\mathbf{D} = d_{iso}\mathbf{I} + d_{ani}\mathbf{n} \otimes \mathbf{n}$  with a pronounced signal propagation along preferred directions  $\mathbf{n}$  [16], which we are currently calibrating by means of in vitro experiments using microelectrode array recordings [15]. The remaining material parameters which are in agreement with the previous example are listed in Table 2. For the sake of simplicity, the entire heart is assumed to be composed of ventricular epicardial cardiomyocytes. Thus, the expected timing and quantitative behavior of different ion concentrations and their currents may not exactly match with what is observed in the actual human heart. However, the incorporation of different cell types is conceptually simple and would require only minor modifications in the finite element input file.

Figs. 7 and 8 illustrate the evolution of the membrane potential  $\phi$  and of the individual ion concentrations  $c_{Na}$ ,  $c_K$  and  $c_{Ca}$  during the depolarization and repolarization phases, respectively. Fig. 7, second row, documents that depolarization is initiated through changes in the intracellular sodium concentration which increases rapidly from 11.60 mM to 11.61 mM within the first 5 ms of the cycle. This increase is associated with a rapid increase in the mem-

brane potential from  $-86$  mV to  $+20$  mV, first row, which, in turn, affects the voltage-gated calcium and potassium channels within the cell membrane. It is primarily through the voltage-gated L-type calcium channel that the intracellular calcium concentration increases from approximately  $0.08$ – $1$   $\mu\text{M}$ , fourth row. Sodium follows with a slight time delay of 15 ms decreasing from 138.30 mM to 138.29 mM, third row. After approximately 30 ms, the entire heart is depolarized and the membrane potential has reached its peak value of 20 mV throughout both ventricles. Fig. 8 displays the repolarization phase characterized through a smooth decrease of the membrane potential back to its initial value of  $-86$  mV after approximately 300 ms, first row. At the same time, the intracellular calcium concentration decreases smoothly back to its resting value of  $0.08$   $\mu\text{M}$ , fourth row. The intracellular sodium concentration that has initially increased from approximately 11.60–11.61 mM is now decreasing even below its initial value and reaches a minimum of 11.585 mM after 280 ms, second row. The intracellular potassium concentration reaches its minimum of 138.29 mM at approximately the same time, third row. In the course of time, both sodium and potassium then slowly return to their resting values as their concentrations increase gradually.

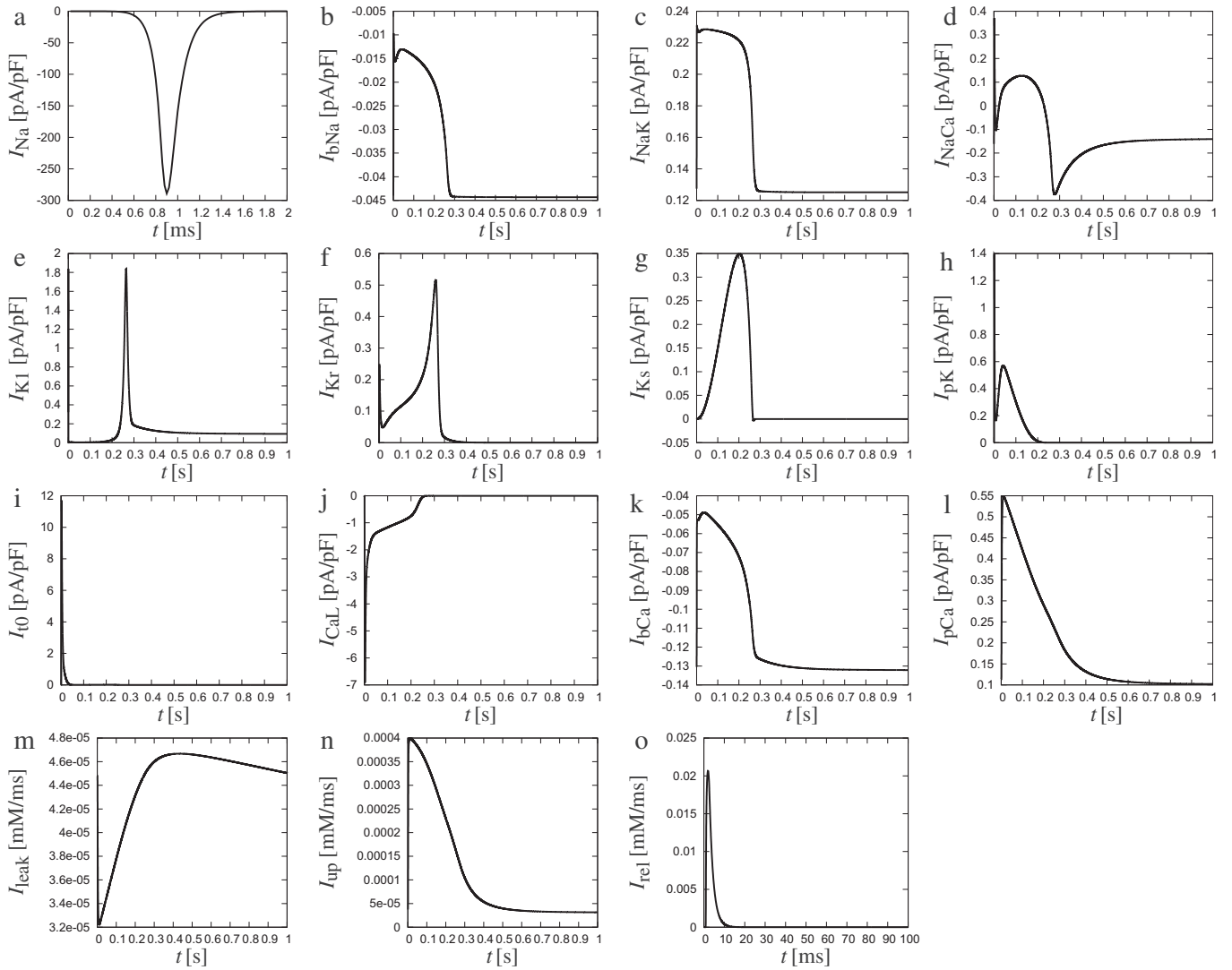


**Fig. 5.** Electrochemistry in a human ventricular cardiomyocyte. Temporal evolution of the fast sodium current  $I_{Na}$ , the background sodium current  $I_{bNa}$ , the sodium potassium pump current  $I_{NaK}$ , and the sodium calcium exchanger current  $I_{NaCa}$ , the inward rectifier current  $I_{K1}$ , the rapid delayed rectifier current  $I_{Kr}$ , the slow delayed rectifier current  $I_{Ks}$ , the plateau potassium current  $I_{pK}$ , the transient outward current  $I_{t0}$ , the L-type calcium current  $I_{CaL}$ , the background calcium current  $I_{bCa}$ , the plateau calcium current  $I_{pCa}$ , the leakage current  $I_{leak}$ , the sarcoplasmic reticulum uptake current  $I_{up}$ , and the sarcoplasmic reticulum release current  $I_{rel}$ .

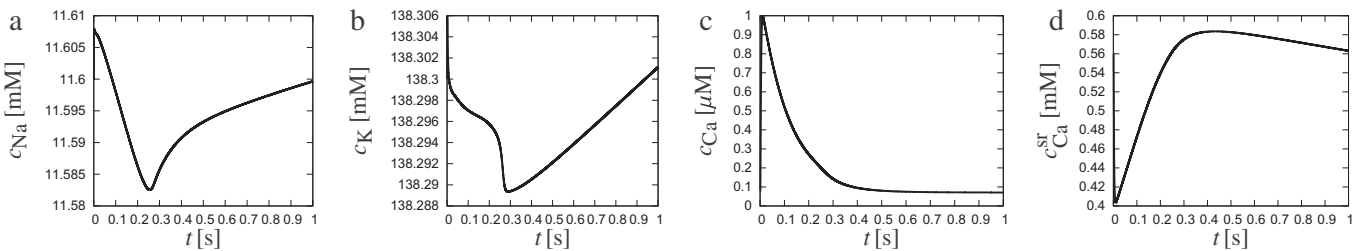


**Fig. 6.** Electrochemistry in a human ventricular cardiomyocyte. Temporal evolution of intracellular sodium concentration  $c_{Na}$ , potassium concentration  $c_K$ , calcium concentration  $c_{Ca}$ , and calcium concentration in the sarcoplasmic reticulum  $c_{Ca}^{SR}$ . The sodium concentration increases rapidly from 11.60 mM to 11.61 mM within the first 5 ms to initiate the fast upstroke of the action potential which then, in turn, affects the voltage-gated calcium and potassium channels. Accordingly, the calcium concentration increases quickly to 1.0  $\mu$ M and then decreases gradually back to its resting value of 0.08  $\mu$ M. The potassium concentration decreases slowly to 138.29 mM until the beginning of the resting phase at after 0.28 s and then gradually returns back to its initial value of 138.30 mM. In this last phase, the sodium concentration which had decreased to 11.585 mM increases gradually to its initial value of 11.60 mM.

These results are in excellent qualitative and quantitative agreement with the single cardiomyocyte results documented in Fig. 6.

Fig. 9 illustrates the algorithmic performance of the proposed algorithm. The top row shows the non-adaptive time stepping

scheme with a fixed time step size of  $\Delta t = 0.125$  ms; the bottom row shows the adaptive time stepping scheme with a maximum time step size of  $\Delta t^{max} = 8.0$  ms. Since we apply a Newton Raphson iteration scheme based on the consistent algorithmic linearization of the governing equations, for both time stepping schemes, we typ-

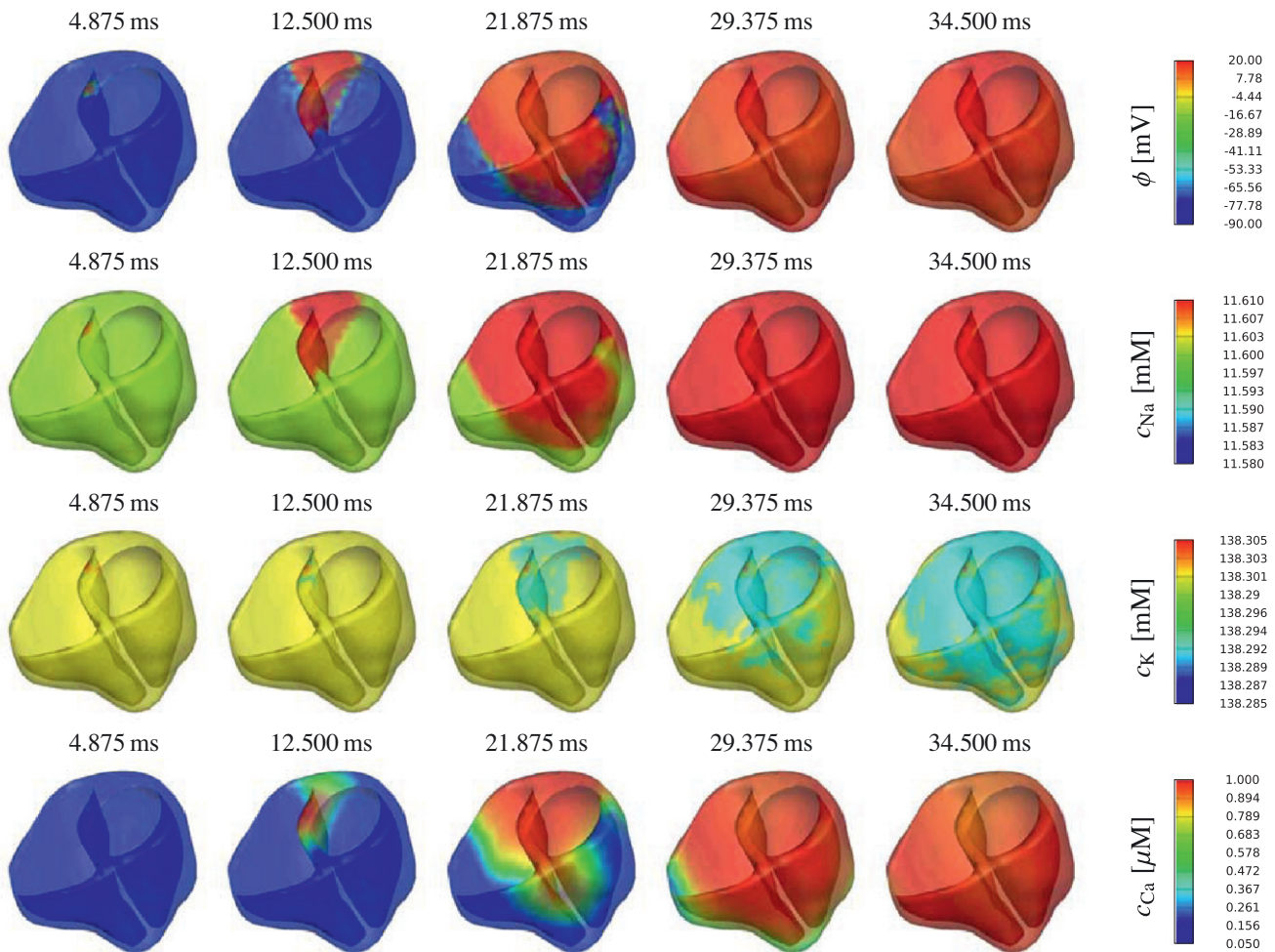


**Fig. 7.** Electrochemistry in the human heart. Spatio-temporal evolution of the membrane potential  $\phi$  and the intracellular sodium, potassium, and calcium concentrations  $c_{Na}$ ,  $c_K$ , and  $c_{Ca}$  during the depolarization phase of the cardiac cycle. Depolarization is initiated through an increase in the intracellular sodium concentration  $c_{Na}$  which reflects itself in the rapid depolarization of the cell characterized through an increase in the membrane potential  $\phi$  from  $-86$  mV to  $+20$  mV. This affects the voltage-gated potassium and calcium channels and initiates a decrease in the intracellular potassium concentration  $c_K$  and an increase in the intracellular calcium concentration  $c_{Ca}$ . After approximately 30 ms, both ventricles of the heart are fully depolarized.

ically find convergence within five to six iterations during the upstroke phase, and within three to four iterations during all other phases of the cardiac cycle. Quadratic convergence of global Newton Raphson iteration is confirmed in Table 3, which documents representative residuals of the relative error during the five different phases of the cardiac cycle. The total run time of an entire cardiac cycle of  $t = 1000$  ms, discretized with 8000 time increments of  $\Delta t = 0.125$  ms for the non-adaptive scheme, is 3845.74 s on a single core of an i7-950 3.06 GHz desktop with 4 GB of memory. Fig. 9, bottom right, demonstrates that the adaptive time stepping scheme automatically increases the time step size during the plateau phase, between  $t = 50$  ms and  $t = 275$  ms, and during the resting phase, after  $t = 350$  ms. This reduces the number of time increments to 492 and the overall run time to 395.46 s. Remarkably, when both models use the same fixed time step, the overall run time of our ionic excitation model is only approximately twice as long as the run time of the two-parameter FitzHugh–Nagumo model [21,39] for which all the information of the chemical problem is lumped into one single phenomenological recovery variable [24,26].

## 7. Discussion

We have presented a novel finite element based algorithm for electrochemical phenomena in cardiac tissue and demonstrated its potential to simulate cardiac excitation in real patient-specific

geometries. In contrast to existing finite difference schemes and collocation methods proposed in the literature, our novel framework is (i) unconditionally stable, (ii) efficient, (iii) highly modular, (iv) geometrically flexible, and (v) easily expandable.

*Unconditional stability* is guaranteed by the use of an implicit backward Euler time integration procedure instead of previously proposed explicit time integration schemes [58]. As a result, our time integration procedure is extremely robust [66], in particular in combination with an incremental iterative Newton Raphson solution technique. A comparison of different time-discretization schemes, explicit, semi-implicit, and implicit, in the context of the phenomenological FitzHugh Nagumo model confirmed that implicit electrophysiological models allow for the largest time step size, however, at the prize of having to invert the system matrix at each iteration step of each time increment [19]. That is why many authors prefer to use of operator splitting [46,54,62] and semi-implicit schemes, in which the nonlinear reaction term is treated explicitly and the diffusion term is treated implicitly [16,64].

*Efficiency* is significantly increased with regard to existing explicit schemes, since we propose a global–local split which only introduces a single global degree of freedom at each finite element node, while all the other state variables are updated locally on the integration point level. In contrast to previous finite element models for electrophysiology, which discretize all unknowns at the finite element nodes [16,37], we adopt the classical finite

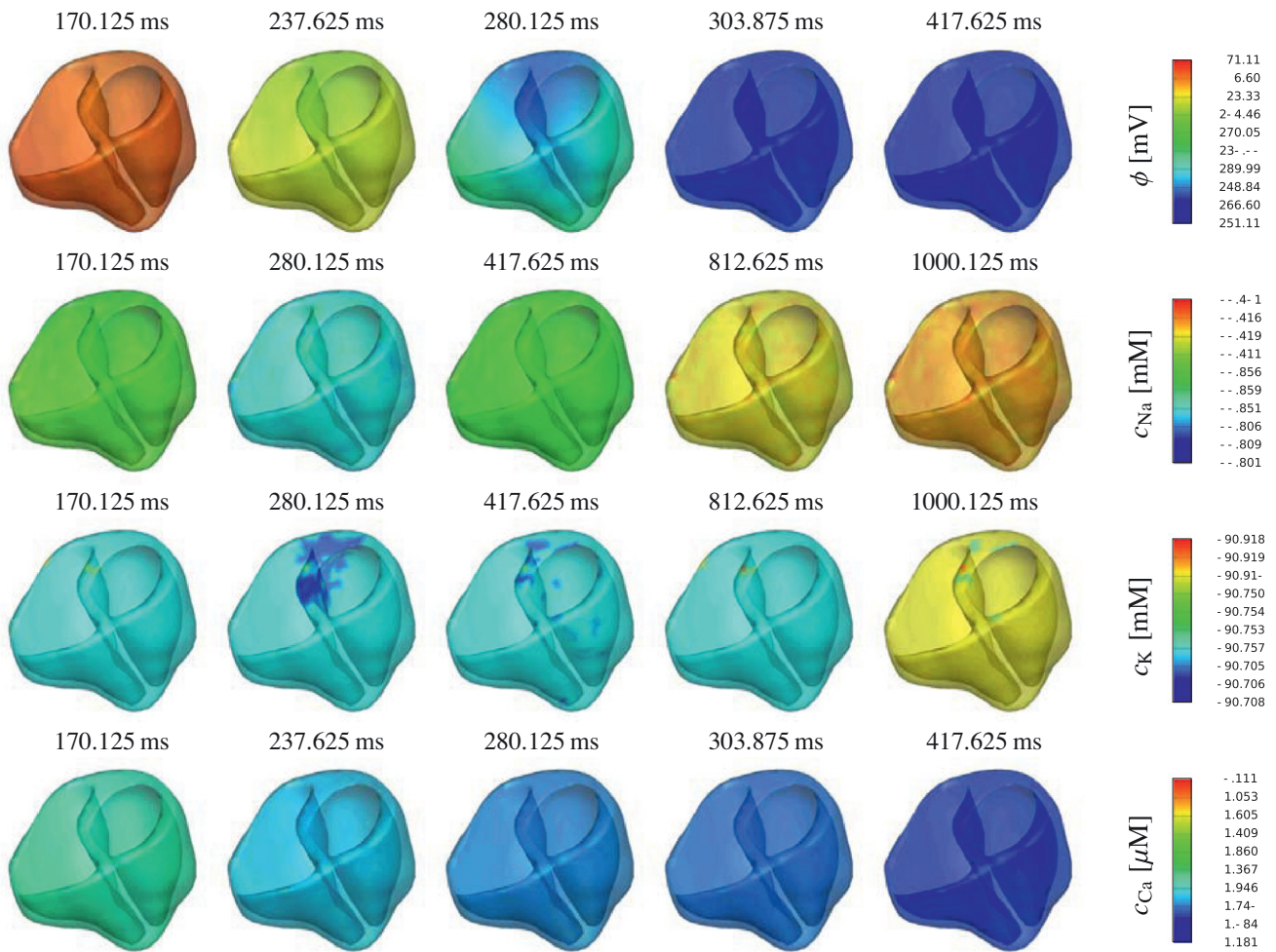


**Fig. 8.** Electrochemistry in the human heart. Spatio-temporal evolution of the membrane potential  $\phi$  and the intracellular sodium, potassium, and calcium concentrations  $c_{Na}$ ,  $c_K$ , and  $c_{Ca}$  during the repolarization phase of the cardiac cycle. Repolarization is characterized through a smooth decrease in the membrane potential  $\phi$  from its excited value of +20 mV back to its resting value of -86 mV. At the same time, the intracellular calcium concentration  $c_{Ca}$  decreases smoothly to its resting value. Both sodium  $c_{Na}$  and potassium  $c_K$  respond more slowly and reach minimum concentrations only after 280 ms before increasing gradually back to their initial values at the end of the cycle after 1000 ms.

element infrastructure of internal variables, which has proven extremely efficient in materially nonlinear continuum mechanics. Following this well-established approach borrowed from nonlinear mechanics, we solve the nonlinear system of equations by means of two nested Newton–Raphson iterations using an existing finite element framework [55], rather than using an inexact Newton or Krylov subspace method as proposed in the literature [37,66]. The use of an implicit time integration scheme, which enables larger time steps than existing explicit schemes [19], further enhances the computational efficiency of our algorithm. It allows us to use simple adaptive time stepping schemes which, in the case shown here, reduce the computational time by more than one order of magnitude.

*Modularity* originates from the particular discretization scheme that treats all unknowns except for the membrane potential as local internal variables on the integration point level. This particular discretization adopts the classical infrastructure of nonlinear finite element programs in continuum mechanics and allows us to recycle a finite element program that was originally designed for structural analysis [55]. Accordingly, the proposed algorithm could be readily integrated into commercial finite element packages by reinterpreting any scalar-valued field, e.g., the temperature field, as the electrical potential field. Algorithmic modifications are restricted exclusively to the constitutive subroutine which would then solve the chemical problem and store the ion concentrations and gating variables as internal variables at each

integration point. Moreover, this modular treatment of the chemical problem enables the straightforward combination of different cell models for pacemaker cells, atrial cells, epicardial ventricular cells, and endocardial ventricular cells, allowing for a fully inhomogeneous description of the underlying cardiac microstructure [1].

*Geometrical flexibility* is the most advantageous feature of finite element techniques when compared to existing finite volume methods or finite difference schemes [38]. Unlike existing schemes which are most powerful on regular grids [11], the proposed finite element based electrochemical model can be applied to arbitrary geometries with arbitrary initial and boundary conditions. It is easily applicable to medical-image based patient-specific geometries [43,65,67,68] as demonstrated in the present manuscript. Here, we have demonstrated the geometric flexibility for a relatively coarse mesh of the heart, which allows us to prototype solutions on single desktop or laptop computers. We are currently investigating the potential of our algorithm when analyzing finer discretizations of the heart. To this end, we adopt the recent parallel version of FEAP [56], which is a modification of the serial version [55], to interface to the PETSc library system available from Argonne National Laboratories.

*Ease of expandability* is probably the most crucial advantage of our algorithm. Being finite element based and modular in nature, our approach lays the groundwork for a robust and stable whole heart model of excitation–contraction coupling [25]. Through a

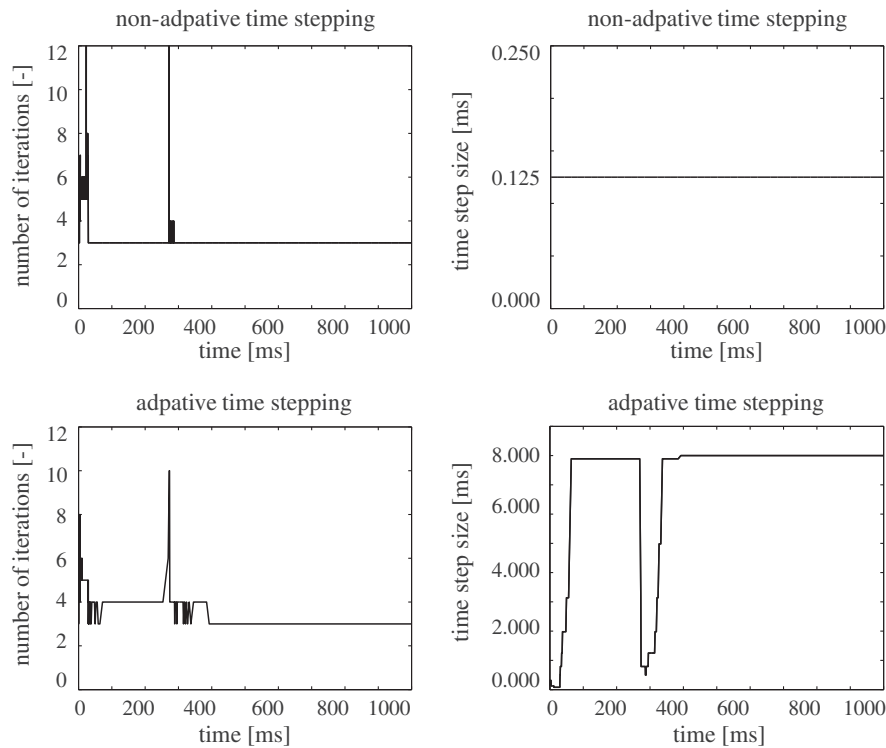


**Fig. 9.** Algorithmic performance. Number of iterations and time step size for non-adaptive and adaptive time stepping schemes. For both algorithms, we typically find convergence within five to six Newton Raphson iterations during the upstroke phase, and within three to four iterations during all other phases of the cardiac cycle. This results in a total run time of 3845.74 s for the non-adaptive scheme with a fixed time step size of  $\Delta t = 0.125$  ms and 8000 time increments throughout the cardiac cycle of  $t = 1000$  ms, calculated on a single core of an i7-950 3.06 GHz desktop with 4 GB of memory. The adaptive time stepping scheme automatically increases the time step size during the plateau phase, between  $t = 50$  ms and  $t = 275$  ms, and during the resting phase, after  $t = 350$  ms. Adaptive time stepping with a maximum time step size of  $\Delta t^{\max} = 8.0$  ms reduces the number of increments to 492, and the overall run time to 395.46 s.

**Table 3**  
Algorithmic performance. Characteristic quadratic convergence of global Newton Raphson iteration, illustrated in terms of the representative residuals of the relative error during five different phases of the cardiac cycle.

	Phase 0 upstroke [28.5 ms]	Phase 1 early repolarization[50 ms]	Phase 2 plateau [150 ms]	Phase 3 final repolarization [250 ms]	Phase 4 resting state[800 ms]
Iteration 1	1.0000000E+00	1.0000000E+00	1.0000000E+00	1.0000000E+00	1.0000000E+00
Iteration 2	2.2132743E-01	5.1643490E-06	3.2776503E-06	7.3800749E-06	3.9746490E-08
Iteration 3	4.2979422E-03	1.5335565E-15	1.0048457E-15	1.0146389E-15	2.7172618E-11
Iteration 4	7.7168299E-06	-	-	-	-
Iteration 5	8.2932031E-11	-	-	-	-

straightforward generalization, the proposed excitation algorithm can easily be coupled to cardiac contraction through the additional incorporation of the mechanical deformation field [8,57]. Also, the incorporation of an additional scalar-valued global unknown for the extracellular potential field is relatively simple, and allows us to extend the proposed formulation to a bidomain model [36,51,52,62]. We have recently undertaken first steps in this direction and have shown that a fully implicit finite element formulation of the bidomain model with two degrees of freedom per finite element node is straightforward within the proposed algorithmic framework [18].

Rather than using phenomenological excitation models which we have successfully applied in the past [24,26], we are now utilizing a more sophisticated ionic excitation model based on observable phenomena on the molecular scale. Although, from an engineering point of view, the number of material parameters required to characterize all individual ion channel activities might seem tremendous, the parameters of this model are related to well-defined electrochemically observable phenomena. The parameter values are extremely well characterized through a huge body of literature on single-cell and single-channel recordings performed within the past decade, see [28,33,45,58] and the refer-

ences cited therein. The use of ionic models will allow us, in the future, to elucidate possible arrhythmogenic phenomena on the molecular and cellular levels. For example, we can now explore the correlation between an enhanced activity of the sodium calcium exchanger  $I_{NaCa}$ , the reduced activity of the sodium potassium pump  $I_{NaK}$ , and prolonged action potential durations typically observable in failing hearts [45]. Along the same lines, we have recently modified our ionic cell model to incorporate a light-activated ion channel, channelrhodopsin, that allows us to activate cardiac cells by photostimulation [1]. This novel technology, which is known as optogenetics, has gained a tremendous popularity in neuroscience within the past decade, and is currently being adopted in cardiology as well. There is hope that optogenetics could be applied to pace the heart with light, and that ionic computational models might provide further insight into optimal pacing parameters. Using the global finite element approach, we will be able to elaborate correlations between alterations in local action potential profiles and global electric activity through the computation of patient-specific electrocardiograms [9,32].

Historically, the electrical excitation problem has been solved with finite difference schemes at a high spatial and temporal resolution. After several electrical time steps, the electric potential is

mapped onto a coarse grid to solve the mechanical problem with finite element methods, to then map the resulting deformation back to the smaller grid [40]. Unfortunately, spatial mapping errors and temporal energy blow up are inherent to this type of solution procedure. We are currently working on a fully coupled monolithic solution of the electro-chemo-mechanical problem for ionic-excitation-contraction coupling that simultaneously solves for the electrical potential, the chemical ion concentrations, and the mechanical deformation in a unique, robust, and efficient way [25,27], see also [13,63]. This framework will allow us to better explain, predict, and prevent rhythm disturbances in the heart. This would have a tremendous potential in the design of novel treatment strategies such as biventricular pacing to prevent heart failure and sudden cardiac death.

## Acknowledgements

The material of this manuscript is based on work supported by the National Science Foundation CAREER award CMMI-0952021 “The Virtual Heart – Exploring the structure–function relationship in electroactive cardiac tissue”. Jonathan Wong was supported through the Biomedical Computation Graduate Training Grant 5T32GM063495-07 and the Sang Samuel Wang Stanford Graduate Fellowship. We thank Dr. Euan Ashley for providing the patient-specific magnetic resonance image, and Anton Dam, Rebecca Taylor, and Daniel Burkhart for their valuable help in meshing the data.

## Appendix A

In this appendix, we will specify the derivatives introduced in Section 5. Locally, on the integration point level, we need to linearize the vector of local residuals  $R_{\text{ion}}^c = [R_K^c, R_{\text{Na}}^c, R_{\text{Ca}}^c, R_{\text{Ca}}^{\text{src}}]$  as defined in Eq. (42) with respect to the vector of ion concentrations  $c_{\text{ion}} = [c_K, c_{\text{Na}}, c_{\text{Ca}}, c_{\text{Ca}}^{\text{src}}]$  to obtain the iteration matrix for the local Newton iteration  $K_{\text{ion}}^c$  as specified in Eq. (43). Globally, on the element level, we need to calculate contributions to the linearization of the source term for the electrical problem  $f^b(\phi, g_{\text{gate}}, c_{\text{ion}})$  defined in Eq. (44) to render the discrete linearization  $d_{\phi} f^b$  as specified in Eq. (45). First, we specify the derivatives of the Nernst potentials  $\phi_{\text{ion}} = [RT]/[Z_{\text{ion}}F] \log(c_{\text{ion}0}/c_{\text{ion}})$  as introduced in Eq. (19), and  $\phi_{\text{KS}} = RT/F \log([c_{\text{K}0} + p_{\text{KNa}}c_{\text{Na}0}]/[c_{\text{K}} + p_{\text{KNa}}c_{\text{Na}}])^{-1}$ .

$$\begin{aligned} d_{c_{\text{ion}}} \phi_{\text{ion}} &= -\frac{RT}{Z_{\text{ion}}F c_{\text{ion}}}, \\ d_{c_{\text{K}}} \phi_{\text{KS}} &= -\frac{RT}{F} \frac{1}{c_{\text{K}} + p_{\text{KNa}}c_{\text{Na}}}, \quad d_{c_{\text{Na}}} \phi_{\text{KS}} = -\frac{RT}{F} \frac{p_{\text{KNa}}}{c_{\text{K}} + p_{\text{KNa}}c_{\text{Na}}}. \end{aligned} \quad (46)$$

In the following four subsections, we will specify the linearizations of the four individual residuals,  $R_{\text{Na}}^c$ ,  $R_K^c$ ,  $R_{\text{Ca}}^c$ , and  $R_{\text{Ca}}^{\text{src}}$  of the evolution equations for the four ion concentrations.

### A.1. Specification of sodium related derivatives

The evolution of the intracellular sodium concentration  $c_{\text{Na}}$  introduced in Eq. (21) and rephrased as residual statement  $R_{\text{Na}}^c \doteq 0$  in Eq. (42.2) obviously depends on the sodium concentration  $c_{\text{Na}}$  itself,

$$d_{c_{\text{Na}}} R_{\text{Na}}^c = 1 + \frac{C}{VF} [d_{c_{\text{Na}}} I_{\text{Na}} + d_{c_{\text{Na}}} I_{\text{bNa}} + 3d_{c_{\text{Na}}} I_{\text{NaK}} + 3d_{c_{\text{Na}}} I_{\text{NaCa}}] \Delta t \quad (47)$$

with the following linearizations of the fast sodium current  $I_{\text{Na}}$ , the background sodium current  $I_{\text{bNa}}$ , and the sodium calcium exchanger current  $I_{\text{NaCa}}$ .

$$\begin{aligned} d_{c_{\text{Na}}} I_{\text{Na}} &= -I_{\text{Na}} \quad d_{c_{\text{Na}}} \phi_{\text{Na}} / [\phi - \phi_{\text{Na}}], \\ d_{c_{\text{Na}}} I_{\text{bNa}} &= -I_{\text{bNa}} \quad d_{c_{\text{Na}}} \phi_{\text{Na}} / [\phi - \phi_{\text{Na}}], \\ d_{c_{\text{Na}}} I_{\text{NaCa}} &= I_{\text{NaCa}} \quad d_{c_{\text{Na}}} \bar{g}_{\text{NaCa}} / \bar{g}_{\text{NaCa}}. \end{aligned} \quad (48)$$

Obviously, the sodium calcium exchanger current  $I_{\text{NaCa}}$  also induces a dependency on the calcium concentration  $c_{\text{Ca}}$

$$d_{c_{\text{Ca}}} R_{\text{Na}}^c = \frac{C}{VF} 3d_{c_{\text{Ca}}} I_{\text{NaCa}} \Delta t \quad (49)$$

with the following linearization of the sodium calcium exchanger current  $I_{\text{NaCa}}$ .

$$d_{c_{\text{Ca}}} I_{\text{NaCa}} = I_{\text{NaCa}} d_{c_{\text{Ca}}} \bar{g}_{\text{NaCa}} / \bar{g}_{\text{NaCa}}. \quad (50)$$

Lastly, the sodium evolution strongly depends on the membrane potential  $\phi$

$$d_{\phi} R_{\text{Na}}^c = \frac{C}{VF} [d_{\phi} I_{\text{Na}} + d_{\phi} I_{\text{bNa}} + 3d_{\phi} I_{\text{NaK}} + 3d_{\phi} I_{\text{NaCa}}] \Delta t, \quad (51)$$

through the voltage-gated fast sodium current  $I_{\text{Na}}$ , the background sodium current  $I_{\text{bNa}}$ , the sodium potassium pump current  $I_{\text{NaK}}$ , and the sodium calcium exchanger current  $I_{\text{NaCa}}$ .

$$\begin{aligned} d_{\phi} I_{\text{Na}} &= I_{\text{Na}} [1 / [\phi - \phi_{\text{Na}}] + 3d_{\phi} g_{\text{m}} / g_{\text{m}} + d_{\phi} g_{\text{h}} / g_{\text{h}} + d_{\phi} g_{\text{j}} / g_{\text{j}}], \\ d_{\phi} I_{\text{bNa}} &= I_{\text{bNa}} 1 / [\phi - \phi_{\text{Na}}], \\ d_{\phi} I_{\text{NaK}} &= I_{\text{NaK}} \quad d_{\phi} \bar{g}_{\text{NaK}} / \bar{g}_{\text{NaK}}, \\ d_{\phi} I_{\text{NaCa}} &= I_{\text{NaCa}} \quad d_{\phi} \bar{g}_{\text{NaCa}} / \bar{g}_{\text{NaCa}}. \end{aligned} \quad (52)$$

In the above linearizations, we have introduced the following abbreviations for the gating-like variables  $\bar{g}_{\text{NaK}}$  and  $\bar{g}_{\text{NaCa}}$ ,

$$\begin{aligned} \bar{g}_{\text{NaK}} &= [1 + 0.1245e^{-0.1\phi F/RT} + 0.0353e^{-\phi F/RT}]^{-1}, \\ \bar{g}_{\text{NaCa}} &= [e^{\gamma\phi F/RT} c_{\text{Na}}^3 c_{\text{Ca}0} - e^{(\gamma-1)\phi F/RT} c_{\text{Na}0}^3 c_{\text{Ca}} \gamma_{\text{NaCa}}] \\ &\quad \times [1 + I_{\text{NaCa}}^{\text{sat}} e^{(\gamma-1)\phi F/RT}]^{-1}, \end{aligned} \quad (53)$$

that govern the activity of the sodium potassium pump current  $I_{\text{NaK}}$  and the sodium calcium exchanger current  $I_{\text{NaCa}}$ .

### A.2. Specification of potassium related derivatives

The intracellular potassium concentration  $c_{\text{K}}$  is governed by the evolution Eq. (26) which has been rephrased as residual statement  $R_K^c \doteq 0$  in Eq. (42.1). It depends on the sodium concentration  $c_{\text{Na}}$

$$d_{c_{\text{Na}}} R_K^c = \frac{C}{VF} [-2d_{c_{\text{Na}}} I_{\text{NaK}} + d_{c_{\text{Na}}} I_{\text{KS}}] \Delta t, \quad (54)$$

through the slow delayed rectifier current  $I_{\text{KS}}$  and through the sodium potassium pump current  $I_{\text{NaK}}$  with their individual linearizations given as follows.

$$\begin{aligned} d_{c_{\text{Na}}} I_{\text{KS}} &= -I_{\text{KS}} d_{c_{\text{Na}}} \phi_{\text{KS}} / [\phi - \phi_{\text{KS}}], \\ d_{c_{\text{Na}}} I_{\text{NaK}} &= I_{\text{NaK}} c_{\text{NaK}} / [c_{\text{Na}} [c_{\text{Na}} + c_{\text{NaK}}]]. \end{aligned} \quad (55)$$

The residual  $R_K^c$  obviously also depends on the potassium concentration  $c_{\text{K}}$  itself

$$d_{c_{\text{K}}} R_K^c = 1 + \frac{C}{VF} [d_{c_{\text{K}}} I_{\text{K1}} + d_{c_{\text{K}}} I_{\text{Kr}} + d_{c_{\text{K}}} I_{\text{KS}} + d_{c_{\text{K}}} I_{\text{pK}} + d_{c_{\text{K}}} I_{\text{t0}}] \Delta t \quad (56)$$

with individual contributions from the inward rectifier current  $I_{\text{K1}}$ , the rapid delayed rectifier current  $I_{\text{Kr}}$ , the slow delayed rectifier current  $I_{\text{KS}}$ , the plateau potassium current  $I_{\text{pK}}$ , and the transient outward current  $I_{\text{t0}}$ .

$$\begin{aligned}
d_{c_K} I_{K1} &= -I_{K1} [d_{c_K} \phi_K / [\phi - \phi_K] + d_{c_K} x_{K1\infty} / x_{K1\infty}], \\
d_{c_K} I_{Kr} &= -I_{Kr} d_{c_K} \phi_K / [\phi - \phi_K], \\
d_{c_K} I_{Ks} &= -I_{Ks} d_{c_K} \phi_{Ks} / [\phi - \phi_{Ks}], \\
d_{c_K} I_{pK} &= -I_{pK} d_{c_K} \phi_K / [\phi - \phi_K], \\
d_{c_K} I_{t0} &= -I_{t0} d_{c_K} \phi_K / [\phi - \phi_K].
\end{aligned} \quad (57)$$

Finally, the potassium residual  $R_{c_K}^c$  strongly depends on the membrane potential  $\phi$

$$d_{\phi} R_{c_K}^c = \frac{C}{VF} [d_{\phi} I_{K1} + d_{\phi} I_{Kr} + d_{\phi} I_{Ks} - 2d_{\phi} I_{NaK} + d_{\phi} I_{pK} + d_{\phi} I_{t0}] \Delta t, \quad (58)$$

through the voltage-gated inward rectifier current  $I_{K1}$ , the rapid delayed rectifier current  $I_{Kr}$ , the slow delayed rectifier current  $I_{Ks}$ , the sodium potassium pump current  $I_{NaK}$ , the plateau potassium current  $I_{pK}$ , and the transient outward current  $I_{t0}$ .

$$\begin{aligned}
d_{\phi} I_{K1} &= I_{K1} [1/[\phi - \phi_K] + d_{\phi} g_{K1}^{\infty} / g_{K1}^{\infty}], \\
d_{\phi} I_{Kr} &= I_{Kr} [1/[\phi - \phi_K] + d_{\phi} g_{xr1} / g_{xr1} + d_{\phi} g_{xr2} / g_{xr2}], \\
d_{\phi} I_{Ks} &= I_{Ks} [1/[\phi - \phi_{Ks}] + 2d_{\phi} g_{xs} / g_{xs}], \\
d_{\phi} I_{NaK} &= I_{NaK} d_{\phi} \bar{g}_{NaK} / \bar{g}_{NaK}, \\
d_{\phi} I_{pK} &= I_{pK} [1/[\phi - \phi_K] + d_{\phi} \bar{g}_{pK} / \bar{g}_{pK}], \\
d_{\phi} I_{t0} &= I_{t0} [1/[\phi - \phi_K] + d_{\phi} g_r / g_r + d_{\phi} g_s / g_s].
\end{aligned} \quad (59)$$

For the sake of compactness, we have introduced the abbreviations for the gating-like variables  $\bar{g}_{NaK}$  and  $\bar{g}_{pK}$ ,

$$\begin{aligned}
\bar{g}_{NaK} &= [e^{\gamma \phi F / RT} c_{Na}^3 c_{Ca0} - e^{(\gamma-1)\phi F / RT} c_{Na0}^3 c_{Ca} \gamma_{NaCa}] \\
&\quad \times [1 + k_{NaCa}^{\text{sat}} e^{(\gamma-1)\phi F / RT}]^{-1}, \\
\bar{g}_{NaK} &= [1 + 0.1245 e^{-0.1\phi F / RT} + 0.0353 e^{-\phi F / RT}]^{-1}, \\
\bar{g}_{pK} &= [1 + e^{(25-\phi)/5.98}]^{-1},
\end{aligned} \quad (60)$$

that govern the activity of the sodium potassium pump current  $I_{NaK}$  and of the plateau potassium current  $I_{pK}$ .

### A.3. Specification of calcium related derivatives

The evolution of the intracellular calcium concentration  $c_{Ca}$  is defined through Eq. (34) or, equivalently, through the corresponding residual statement  $R_{c_{Ca}}^c \doteq 0$  introduced in Eq. (42.3). This residual depends on the sodium concentration  $c_{Na}$

$$d_{c_{Na}} R_{c_{Ca}}^c = \gamma_{Ca} \frac{C}{2VF} [-2d_{c_{Na}} I_{NaCa}] \Delta t, \quad (61)$$

through the sodium calcium exchanger current  $I_{NaCa}$ .

$$d_{c_{Ca}} I_{NaCa} = I_{NaCa} d_{c_{Ca}} \bar{g}_{NaCa} / \bar{g}_{NaCa}. \quad (62)$$

Obviously, the residual  $R_{c_{Ca}}^c$  also depends on the calcium concentration  $c_{Ca}$  itself,

$$\begin{aligned}
d_{c_{Ca}} R_{c_{Ca}}^c &= 1 + \gamma_{Ca} \left[ \frac{C}{2VF} [d_{c_{Ca}} I_{CaL} + d_{c_{Ca}} I_{bCa} + d_{c_{Ca}} I_{pCa} \right. \\
&\quad \left. - 2d_{c_{Ca}} I_{NaCa}] - d_{c_{Ca}} I_{leak} + d_{c_{Ca}} I_{up} - d_{c_{Ca}} I_{rel}] \Delta t \right. \\
&\quad \left. + d_{\phi} \gamma_{Ca} \left[ \frac{C}{2VF} [I_{CaL} + I_{bCa} + I_{pCa} - 2I_{NaCa}] \right. \right. \\
&\quad \left. \left. - I_{leak} + I_{up} - I_{rel}] \Delta t, \right. \right. \quad (63)
\end{aligned}$$

on the one hand through the L-type calcium current  $I_{CaL}$ , the background calcium current  $I_{bCa}$ , the plateau calcium current  $I_{pCa}$ , the sodium calcium pump current  $I_{NaCa}$ , the leakage current  $I_{leak}$ , the sarcoplasmic reticulum uptake current  $I_{up}$ , and the sarcoplasmic reticulum release current  $I_{rel}$ ,

$$\begin{aligned}
d_{c_{Ca}} I_{CaL} &= I_{CaL} [d_{c_{Ca}} g_{fCa} / g_{fCa} + d_{c_{Ca}} \bar{g}_{CaL} / \bar{g}_{CaL}], \\
d_{c_{Ca}} I_{bCa} &= I_{bCa} d_{c_{Ca}} \phi_{Ca} / [\phi - \phi_{Ca}], \\
d_{c_{Ca}} I_{pCa} &= I_{pCa} [c_{pCa} + c_{Ca}]^{-1} c_{pCa} / c_{Ca}, \\
d_{c_{Ca}} I_{NaCa} &= I_{NaCa} d_{c_{Ca}} \bar{g}_{NaCa} / \bar{g}_{NaCa}, \\
d_{c_{Ca}} I_{leak} &= -J_{leak}^{\text{max}}, \\
d_{c_{Ca}} I_{up} &= I_{up} [1 + c_{up}^2 / c_{Ca}^2]^{-1} 2c_{up}^2 / c_{Ca}^3, \\
d_{c_{Ca}} I_{rel} &= I_{rel} d_{c_{Ca}} g_g / g_g
\end{aligned} \quad (64)$$

and on the other hand through the weighting coefficient  $\gamma_{Ca} = [1 + [c_{totCa}][c_{Ca} + c_{buf}]^{-2}]^{-1}$  which is relating the free intracellular calcium concentration to the total intracellular calcium concentration. The residual  $R_{c_{Ca}}^c$  further directly depends on the calcium concentration in the sarcoplasmic reticulum  $c_{Ca}^{\text{sr}}$

$$d_{c_{Ca}^{\text{sr}}} R_{c_{Ca}}^c = \gamma_{Ca} [-d_{c_{Ca}^{\text{sr}}} I_{leak} - d_{c_{Ca}^{\text{sr}}} I_{rel}] \Delta t, \quad (65)$$

through the leakage current  $I_{leak}$  and through the release current  $I_{rel}$ .

$$\begin{aligned}
d_{c_{Ca}^{\text{sr}}} I_{leak} &= I_{leak}^{\text{max}}, \\
d_{c_{Ca}^{\text{sr}}} I_{rel} &= I_{rel} d_{c_{Ca}^{\text{sr}}} \bar{g}_{rel} / \bar{g}_{rel}.
\end{aligned} \quad (66)$$

Lastly, the evolution of the intracellular calcium concentration strongly depends on the membrane potential  $\phi$

$$d_{\phi} R_{c_{Ca}} = \gamma_{Ca} \left[ \frac{C}{2VF} [d_{\phi} I_{CaL} + d_{\phi} I_{bCa} - 2d_{\phi} I_{NaCa}] - d_{\phi} I_{rel} \right] \Delta t, \quad (67)$$

through the voltage-gated L-type calcium current  $I_{CaL}$ , the background calcium current  $I_{bCa}$ , the sodium calcium exchanger current  $I_{NaCa}$ , and the sarcoplasmic reticulum release current  $I_{rel}$ .

$$\begin{aligned}
d_{\phi} I_{CaL} &= I_{CaL} [d_{\phi} g_f / g_f + d_{\phi} g_d / g_d + d_{\phi} \bar{g}_{CaL} / \bar{g}_{CaL}], \\
d_{\phi} I_{bCa} &= C_{bCa}^{\text{max}}, \\
d_{\phi} I_{rel} &= I_{rel} d_{\phi} g_d / g_d.
\end{aligned} \quad (68)$$

Again, we have used abbreviations for the gating-like variables  $\bar{g}_{NaCa}$ ,  $\bar{g}_{CaL}$ , and  $\bar{g}_{rel}$ ,

$$\begin{aligned}
\bar{g}_{NaCa} &= [e^{\gamma \phi F / RT} c_{Na}^3 c_{Ca0} - e^{(\gamma-1)\phi F / RT} c_{Na0}^3 c_{Ca} \gamma_{NaCa}] [1 + k_{NaCa}^{\text{sat}} e^{(\gamma-1)\phi F / RT}]^{-1}, \\
\bar{g}_{CaL} &= [4\phi F^2] / [RT] [c_{Ca} e^{2\phi F / RT} - 0.341 c_{Ca0}] [e^{2\phi F / RT} - 1]^{-1}, \\
\bar{g}_{rel} &= 1 + \gamma_{rel} c_{Ca}^{\text{sr}2} [c_{rel}^2 + c_{Ca}^{\text{sr}2}]^{-1},
\end{aligned} \quad (69)$$

that govern the activity of the sodium calcium exchanger current  $I_{NaCa}$ , of the L-type calcium current  $I_{CaL}$ , and of the sarcoplasmic reticulum release current  $I_{rel}$ .

### A.4. Specification of sarcoplasmic reticulum calcium related derivatives

Last, we specify the linearizations related to the evolution equation for the calcium concentration in the sarcoplasmic reticulum (40) which has been rephrased as residual statement  $R_{c_{Ca}^{\text{sr}}} \doteq 0$  in Eq. (42.4). Its residual depends on the intracellular calcium concentration  $c_{Ca}$ ,

$$d_{c_{Ca}} R_{c_{Ca}^{\text{sr}}} = \gamma_{Ca}^{\text{sr}} \frac{V}{V^{\text{sr}}} [d_{c_{Ca}} I_{leak} - d_{c_{Ca}} I_{up} + d_{c_{Ca}} I_{rel}] \Delta t, \quad (70)$$

on the calcium concentration in the sarcoplasmic reticulum  $c_{Ca}^{\text{sr}}$ ,

$$d_{c_{Ca}^{\text{sr}}} R_{c_{Ca}^{\text{sr}}} = 1 + \gamma_{Ca}^{\text{sr}} \frac{V}{V^{\text{sr}}} [d_{c_{Ca}^{\text{sr}}} I_{leak} + d_{c_{Ca}^{\text{sr}}} I_{rel} + [I_{leak} - I_{up} + I_{rel}] d_{c_{Ca}^{\text{sr}}} \gamma_{Ca}^{\text{sr}}] \Delta t \quad (71)$$

and on the membrane potential  $\phi$ .

$$d_{\phi} R_{Ca}^{Sr} = \gamma_{Ca}^{Sr} \frac{V}{V^{Sr}} d_{\phi} I_{rel} \Delta t. \quad (72)$$

Recall that the weighting coefficient  $\gamma_{Ca}^{Sr} = [1 + \frac{[c_{tot}^{Sr}]}{[c_{buf}^{Sr}]}]^{-1}$ , which has to be linearized to evaluate Eq. (71), is relating the free calcium concentration to the total calcium concentration in the sarcoplasmic reticulum.

## References

- [1] O.J. Abilez, J. Wong, R. Prakash, K. Deisseroth, C.K. Zarins, E. Kuhl, Multiscale computational models for optogenetic control of cardiac function, *Biophys. J.* 101 (2011), in press.
- [2] American Heart Association, Heart Disease and Stroke Statistics – 2010 Update, Dallas, Texas: American Heart Association, 2010.
- [3] R.R. Aliev, A.V. Panfilov, A simple two-variable model of cardiac excitation, *Chaos Solitons Fract.* 7 (1996) 293–301.
- [4] G.W. Beeler, H. Reuter, Reconstruction of the action potential of ventricular myocardial fibers, *J. Physiol.* 268 (1977) 177–210.
- [5] R.M. Berne, M.N. Levy, Cardiovascular physiology, The Mosby Monograph Seri. (2001).
- [6] O. Bernus, R. Wilders, C.W. Zemlin, H. Verschele, A.V. Panfilov, A computationally efficient electrophysiological model of human ventricular cells, *Am. J. Physiol. Heart Circ. Physiol.* 282 (2002) H2296–H2308.
- [7] M.D. Bers, Excitation-Contraction Coupling and cardiac Contractile Force, Kluwer Academic Publishers, 2001.
- [8] M. Böl, S. Reese, K.K. Parker, E. Kuhl, Computational modeling of muscular thin films for cardiac repair, *Comput. Mech.* 43 (2009) 535–544.
- [9] M. Boulakia, S. Cazeau, M.A. Fernandez, J.F. Gerbeau, N. Zemzemi, Mathematical modeling of electrocardiograms: A numerical study, *Ann. Biomed. Engrg.* 38 (2010) 1071–1097.
- [10] E. Braunwald, Heart Disease: A Textbook of Cardiovascular Medicine, W.B. Saunders Co, Philadelphia, 1997.
- [11] M. Brera, J.W. Jerome, Y. Mori, R. Sacco, A conservative and monotone mixed-hybridized finite element approximation of transport problems in heterogeneous domains, *Comput. Methods Appl. Mech. Engrg.* 199 (2010) 2709–2720.
- [12] S.L. Caffrey, P.J. Willoughby, P.E. Pepe, L.B. Becker, Public use of automated external defibrillators, *N. Engl. J. Med.* 347 (2002) 1242–1247.
- [13] D. Chapelle, M.A. Fernandez, J.F. Gerbeau, P. Moireau, J. Sainte-Marie, N. Zemzemi, Numerical simulation of the electromechanical activity of the heart, *Lecture Notes in Computer Science*, vol. 5528, Springer-Verlag, 2009.
- [14] R.H. Clayton, A.V. Panfilov, A guide to modelling cardiac electrical activity in anatomically detailed ventricles, *Progr. Biophys. Mol. Biol.* 96 (2008) 19–43.
- [15] M.Q. Chen, J. Wong, E. Kuhl, L.B. Giovannardi, G.T.A. Kovacs, Characterization of electrophysiological conduction in cardiomyocyte co-cultures using co-occurrence analysis, submitted for publication.
- [16] P. Colli Franzone, L.F. Pavarino, A parallel solver for reaction-diffusion systems in computational electrocardiology, *Math. Mod. Methods Appl. Sci.* 14 (2004) 883–911.
- [17] M. Courtemanche, R.J. Ramirez, S. Nattel, Ionic mechanisms underlying human atrial action potential properties: Insights from a mathematical model, *Am. J. Physiol. Heart Circ. Physiol.* 275 (1998) 301–321.
- [18] H. Dal, S. Göktepe, M. Kaliske, E. Kuhl, A fully implicit finite element method for bidomain models of cardiac electrophysiology, *Comput. Methods Biomech. Biomed. Engrg.*, in press, doi:10.1080/10255842.2011.554410.
- [19] M. Ethier, Y. Bourgault, Semi-implicit time-discretization schemes for the bidomain model, *SIAM J. Numer. Anal.* 46 (2008) 2443–2468.
- [20] D. DiFrancesco, D. Noble, A model of cardiac electrical activity incorporating ionic pumps and concentration changes, *Philos. Trans. R. Soc. Lond. Biol. Sci.* 307 (1985) 353–398.
- [21] R. FitzHugh, Impulses and physiological states in theoretical models of nerve membranes, *Biophys. J.* 1 (1961) 445–466.
- [22] L. Galvani, De viribus electricitatis in motu musculari commentarius. De Bononiensi Scientiarum et Artium Instituto atque Academia Commentarii. Ex Typographia Institutii Scientiarum, Bononiae, vol VII, 1791, pp. 363–418.
- [23] W.F. Ganong, Review of Medical Physiology, McGraw-Hill/ Appleton & Lange, 2003.
- [24] S. Göktepe, E. Kuhl, Computational modeling of electrophysiology: A novel finite element approach, *Int. J. Numer. Methods Engrg.* 79 (2009) 156–178.
- [25] S. Göktepe, E. Kuhl, Electromechanics of the heart - A unified approach to the strongly coupled excitation-contraction problem, *Comput. Mech.* 45 (2010) 227–243.
- [26] S. Göktepe, J. Wong, E. Kuhl, Atrial and ventricular fibrillation - Computational simulation of spiral waves in cardiac tissue, *Arch. Appl. Mech.* 80 (2010) 569–580.
- [27] S. Göktepe, S.N.S. Acharya, J. Wong, E. Kuhl, Computational modeling of passive myocardium, *Int. J. Numer. Methods Biomed. Engrg.* 27 (2011) 1–12.
- [28] J.L. Greenstein, R.L. Winslow, An integrative model of the cardiac ventricular myocyte incorporating local control of  $Ca^{2+}$  release, *Biophys. J.* 83 (2002) 2918–2945.
- [29] A.L. Hodgkin, A.F. Huxley, A quantitative description of membrane current and its application to conductance and excitation in nerve, *J. Physiol.* 117 (1952) 500–544.
- [30] H.V. Huikuri, A. Castellanos, R.J. Myerburg, Medical progress: Sudden death due to cardiac arrhythmias, *N. Engl. J. Med.* 345 (2001) 1473–1482.
- [31] J. Keener, J. Sneyd, Mathematical Physiology, Springer Science and Business Media, 2004.
- [32] M. Kotikanyadanam, S. Göktepe, E. Kuhl, Computational modeling of electrocardiograms - A finite element approach towards cardiac excitation, *Int. J. Numer. Methods Biomed. Engrg.* 26 (2010) 524–533.
- [33] C.H. Luo, Y. Rudy, A model of the ventricular cardiac action potential. Depolarization, repolarization, and their changes, *Circ. Res.* 68 (1991) 1501–1526.
- [34] C.H. Luo, Y. Rudy, A dynamic model of the cardiac ventricular action potential. I. Simulations of ionic currents and concentration changes, *Circ. Res.* 74 (1994) 1071–1096.
- [35] R.E. McAllister, D. Noble, R.W. Tsien, Reconstruction of the electrical activity of cardiac Purkinje fibres, *J. Physiol.* 251 (1975) 1–59.
- [36] L. Mirabella, F. Nobile, A. Venezi, An a posteriori error estimator for model adaptivity in electrocardiology, *Comput. Methods Appl. Mech. Engrg.*, in press, doi:10.1016/j.cma.2010.03.009.
- [37] M. Munteanu, L.F. Pavarino, Decoupled Schwarz algorithms for implicit discretizations of nonlinear monodomain and bidomain systems, *Math. Mod. Methods Appl. Sci.* 19 (2009) 1065–1097.
- [38] M. Murillo, X.C. Cai, A fully implicit parallel algorithm for simulating the nonlinear electrical activity of the heart, *Numer. Lin. Alg. Appl.* 11 (2004) 261–277.
- [39] J. Nagumo, S. Arimoto, S. Yoshizawa, Active pulse transmission line simulating nerve axon, *Proc. Inst. Radio Engr.* 50 (1962) 2061–2070.
- [40] M.P. Nash, A.V. Panfilov, Electromechanical model of excitable tissue to study reentrant cardiac arrhythmias, *Progr. Biophys. Mol. Biol.* 85 (2004) 501–522.
- [41] D. Noble, A modification of the Hodgkin-Huxley equations applicable to Purkinje fibre action and pacemaker potentials, *J. Physiol.* 160 (1962) 317–352.
- [42] L.H. Opie, Heart Physiology: From Cell to Circulation, Lippincott Williams & Wilkins, 2003.
- [43] G. Plank, R.A.B. Burton, P. Hales, M. Bishop, T. Mansoori, M.O. Bernabeu, A. Garny, A.J. Prassl, C. Bollensdorff, F. Mason, F. Mahmood, B. Rodriguez, V. Grau, J.E. Schneider, G. Gavaghan, P. Kohl, Generation of histo-anatomically representative models of the individual heart: tools and application, *Philos. Trans. R. Soc. A – Math. Phys. Engrg. Sci.* 367 (2009) 2257–2292.
- [44] R. Plonsey, R.C. Barr, Bioelectricity, A Quantitative Approach, Springer Science and Business Media, 2007.
- [45] L. Priebe, D.J. Beuckelmann, Simulation study of cellular electric properties in heart failure, *Circ. Res.* 82 (1998) 1206–1223.
- [46] Z. Qu, A. Garfinkel, An advanced algorithm for solving partial differential equations in cardiac conduction, *IEE Trans. Biomed. Engrg.* 46 (1999) 1166–1168.
- [47] J.M. Rogers, A.D. McCulloch, A collocation-Galerkin finite element model of cardiac action potential propagation, *IEEE Trans. Biomed. Engrg.* 41 (1994) 743–757.
- [48] J.M. Rogers, Wave front fragmentation due to ventricular geometry in a model of the rabbit heart, *Chaos* 12 (2002) 779–787.
- [49] S. Rush, H. Larsen, Practical algorithm for solving dynamic membrane equations, *IEEE Trans. Biomed. Engrg.* 25 (1978) 389–392.
- [50] F.B. Sachse, Computational Cardiology, Springer Verlag, 2004.
- [51] S. Scacchi, A hybrid multilevel Schwarz method for the bidomain model, *Comput. Methods Appl. Mech. Engrg.* 197 (2008) 4051–4061.
- [52] S. Scacchi, A multilevel hybrid Newton-Krylov-Schwarz method for the bidomain model of electrocardiology, *Comput. Methods Appl. Mech. Engrg.*, in press, doi:10.1016/j.cma.2010.09.016.
- [53] M. Sermesant, K. Rhode, G.I. Sanchez-Ortiz, O. Camara, R. Andriantsimiavona, S. Hegde, D. Rueckert, P. Lambiase, C. Bucknall, E. Rosenthal, H. Delingette, D.L.G. Hill, N. Ayache, R. Razavi, Simulation of cardiac pathologies using an electromechanical biventricular model and XMR interventional imaging, *Med. Im. Anal.* 9 (2005) 467–480.
- [54] J. Sundnes, G.T. Lines, A. Tveito, An operator splitting method for solving the bidomain equations coupled to a volume conductor model for the torso, *Math. Biosci.* 194 (2005) 233–248.
- [55] R.L. Taylor, FEAP - A Finite Element Analysis Program, Version 8.3, User Manual, University of California at Berkeley, 2011.
- [56] R.L. Taylor, S. Govindjee, FEAP - A Finite Element Analysis Program, Version 8.3, Parallel User Manual, University of California at Berkeley, 2011.
- [57] A. Tsamis, W. Bothe, J.P. Kitting, J.C. Swanson, D.C. Miller, E. Kuhl, Active contraction of cardiac muscle: In vivo characterization of mechanical activation sequences in the beating heart, *J. Mech. Behavior Biomed. Mat.* 4 (2011) 1167–1176.
- [58] K.H.W.J. ten Tusscher, D. Noble, P.J. Noble, A.V. Panfilov, A model for human ventricular cardiomyocytes, *Am. J. Physiol. Heart Circ. Physiol.* 286 (2004) H1573–H1589.
- [59] K.H.W.J. ten Tusscher, A.V. Panfilov, Cell model for efficient simulation of wave propagation in human ventricular tissue under normal and pathological conditions, *Phys. Med. Biol.* 51 (2006) 6141–6156.
- [60] K.H.W.J. ten Tusscher, O. Bernus, R. Hren, A.V. Panfilov, Comparison of electrophysiological models for human ventricular cells and tissues, *Progr. Biophys. Mol. Bio.* 90 (2006) 326–345.
- [61] K.H.W.J. ten Tusscher, A.V. Panfilov, Modelling of the ventricular conduction system, *Progr. Biophys. Mol. Bio.* 96 (2008) 152–170.
- [62] E.J. Vigmond, F. Aquel, N.A. Trayanova, Computational techniques for solving the bidomain equations in three dimensions, *IEE Trans. Biomed. Engrg.* 49 (2002) 1260–1269.

- [63] D.K. Vu, P. Steinmann, A 2-D coupled BEM-FEM simulation of electro-elastostatics at large strain, *Comput. Methods Appl. Mech. Engrg.* 199 (2010) 1124–1133. *Philos. Trans. R. Soc. A-Math. Phys. Eng. Sci.*
- [64] J.P. Whiteley, An efficient numerical technique for the solution of the monodomain and bidomain equations, *IEEE Trans. Biomed. Engrg.* 53 (2006) 2139–2147.
- [65] D. Weiss, M. Iffland, F.B. Sachse, G. Seemann, O. Dössel, Modeling of cardiac ischemia in human myocytes and tissue including spatiotemporal electrophysiological variations, *Biomed. Tech.* 54 (2009) 107–125.
- [66] W. Ying, D.J. Rose, C.S. Henriquez, Efficient fully implicit time integration methods for modeling cardiac dynamics, *IEEE Trans. Biomed. Engrg.* 55 (2008) 2701–2711.
- [67] Y. Zhang, C. Bajaj, B.S. Sohn, 3D finite element meshing from imaging data, *Comput. Methods Appl. Mech. Engrg.* 194 (2005) 5083–5106.
- [68] Y. Zhang, Y. Bazilevs, S. Goswami, C.L. Bajaj, T.J.R. Hughes, Patient-specific vascular NURBS modeling for isogeometric analysis of blood flow, *Comput. Methods Appl. Mech. Engrg.* 196 (2007) 2943–2959.
- [69] Z. Zheng, J. Croft, W. Giles, G. Mensah, Sudden cardiac death in the United States, *Circulation* 104 (2001) 2158–2163.